

Diagnostic-Photographic Determination of Drag/Lift/Torque Coefficients of High Speed Rigid Body in Water Column

Peter C. Chu and Chenwu Fan

*Naval Ocean Analysis and Prediction Laboratory
Naval Postgraduate School, Monterey, California*

Paul R. Gefken

Polter Laboratory, SRI International, Menlo Park, California

Report Documentation Page				Form Approved OMB No. 0704-0188	
Public reporting burden for the collection of information is estimated to average 1 hour per response, including the time for reviewing instructions, searching existing data sources, gathering and maintaining the data needed, and completing and reviewing the collection of information. Send comments regarding this burden estimate or any other aspect of this collection of information, including suggestions for reducing this burden, to Washington Headquarters Services, Directorate for Information Operations and Reports, 1215 Jefferson Davis Highway, Suite 1204, Arlington VA 22202-4302. Respondents should be aware that notwithstanding any other provision of law, no person shall be subject to a penalty for failing to comply with a collection of information if it does not display a currently valid OMB control number.					
1. REPORT DATE 2008		2. REPORT TYPE		3. DATES COVERED 00-00-2008 to 00-00-2008	
4. TITLE AND SUBTITLE Diagnostic-Photographic Determination of Drag/Lift/Torque Coefficients of High Speed Rigid Body in Water Column				5a. CONTRACT NUMBER	
				5b. GRANT NUMBER	
				5c. PROGRAM ELEMENT NUMBER	
6. AUTHOR(S)				5d. PROJECT NUMBER	
				5e. TASK NUMBER	
				5f. WORK UNIT NUMBER	
7. PERFORMING ORGANIZATION NAME(S) AND ADDRESS(ES) Naval Ocean Analysis and Prediction Laboratory,Naval Postgraduate School,Monterey ,CA				8. PERFORMING ORGANIZATION REPORT NUMBER	
9. SPONSORING/MONITORING AGENCY NAME(S) AND ADDRESS(ES)				10. SPONSOR/MONITOR'S ACRONYM(S)	
				11. SPONSOR/MONITOR'S REPORT NUMBER(S)	
12. DISTRIBUTION/AVAILABILITY STATEMENT Approved for public release; distribution unlimited					
13. SUPPLEMENTARY NOTES					
14. ABSTRACT					
15. SUBJECT TERMS					
16. SECURITY CLASSIFICATION OF:			17. LIMITATION OF ABSTRACT Same as Report (SAR)	18. NUMBER OF PAGES 50	19a. NAME OF RESPONSIBLE PERSON
a. REPORT unclassified	b. ABSTRACT unclassified	c. THIS PAGE unclassified			

Abstract

Prediction of rigid body falling through water column with a high speed (such as Mk-84 bomb) needs formulas for drag/lift and torque coefficients, which depend on various physical processes such as supercavitation and bubbles. A diagnostic-photographic method is developed in this study to determine the drag/lift and torque coefficients for a fast moving rigid-body in water column. The diagnostic part is to derive the relationships (called diagnostic relationships) between (drag, lift, torque) coefficients and (position, orientation) of the rigid body from the three momentum equations and three moment of momentum equations. The photographic part is to collect data of trajectory and orientation of a fast moving rigid body using multiple high-speed video cameras (10,000 Hz). Substitution of the digital photographic data into the diagnostic relationships leads to semi-empirical formulas of drag/lift and torque coefficients, which are functions of the Reynolds number, attack angle, and rotation rate. This method was verified by 1/12th Mk-84 bomb strike experiment with various tail configurations (tail section with four fins, two fins, and no fin and no tail section) conducted at the SRI test site. The cost of this method is much lower than the traditional method using the wind tunnel. Various trajectory patterns are found for different tail configurations.

Keywords: Body-flow interaction, drag coefficient, lift coefficient, torque coefficient, fast rigid body in water column, dynamic-photographic method

1. Introduction

Prediction of a fast moving rigid body in water column has wide scientific significance and technical application. The dynamics of a rigid body allows one to set up six nonlinear equations for the most general motion: three momentum equations and three moment-of-momentum equations. The scientific studies of the hydrodynamic characteristics of a rigid body in water column involve nonlinear dynamics, body and multi-phase fluid interaction, supercavitation, and instability theory.

The technical application of the hydrodynamics of a rigid body with high speed into fluid includes aeronautics, navigation, and civil engineering. Recently, the scientific problem about the movement of a rigid body in water column drew attention to the naval research. This is due to the threat of mine and maritime improvised explosive device (IED). Prediction of a fast falling rigid body in the water column contributes to the bomb breaching for mine/maritime IED clearance in surf and very shallow water zones depth shallower than 12.2 m (i.e., 40 ft), according to U.S. Navy's standards.

To predict rigid body maneuvering in water column, accurate calculation of hydrodynamic forces and torques is important but difficult. Difficulty is caused by unknown drag, lift, and torque coefficients. Thus, determination of these coefficients is crucial for the prediction^{[1][2][3]}. Different from traditional methods used in aerodynamics such as using the wind tunnel, we present a new efficient and low cost method to determine the drag, lift, torque coefficients. This method consists of dynamical and photographic parts. The dynamical part is to establish diagnostic relationships between hydrodynamic coefficients (e.g., drag, lift, torque coefficients) and kinematics of the rigid body (e.g., position, orientation). The photographic part is to conduct experiments with

shooting the rigid body into the hydrographical tank with high speed and recording its underwater position and orientation with high-speed video (HSV) cameras at 10,000 films per second (fps). Semi-empirical formulas can be established for the drag, lift, torque coefficients by substituting the digital data of rigid body's location and orientation from the HSV cameras into the diagnostic relationships.

The rest of the paper is outlined as follows. Sections 2 and describes hydrodynamic forces/torques and basic dynamics. Section 4 presents the diagnostic relationships for the drag/lift and torque coefficients, which were derived from the momentum and moment of momentum equations. Section 5 depicts the photographic method. Sections 6 and 7 show the semi-empirical formulas for the drag/lift and torque coefficients and the verification. Section 8 describes the tail section damage effects. Section 9 presents the conclusions.

2. Hydrodynamic Forces and Torques

2.1. Drag/Lift Forces

Let the earth-fixed coordinate system is use with (\mathbf{i}, \mathbf{j}) the unit vectors in the horizontal plane and \mathbf{k} the unit vector in the vertical direction. Consider an axially symmetric rigid body such as a bomb falling through water column. The two end-points of the body (i.e., head and tail points) are represented by $\mathbf{r}_h(t)$ and $\mathbf{r}_t(t)$. The difference between the two vectors in nondimensional form

$$\mathbf{e} = \frac{\mathbf{r}_h - \mathbf{r}_t}{|\mathbf{r}_h - \mathbf{r}_t|}, \quad (1)$$

is the unit vector representing the body's main axis direction (Fig. 1). The centers of mass (o_m) and volume (o_v) are located on the main axis with σ the distance between o_v and o_m , which has a positive (negative) value when the direction from o_v to o_m is the same

(opposite) as the unit vector \mathbf{e} (Fig. 2). The location (or called translation) of the body is represented by the position of o_m ,

$$\mathbf{r}(t) = x\mathbf{i} + y\mathbf{j} + z\mathbf{k}. \quad (2)$$

The translation velocity is given by

$$\frac{d\mathbf{r}_o}{dt} = \mathbf{u}, \quad \mathbf{u} = U\mathbf{e}_u, \quad (3)$$

where (U, \mathbf{e}_u) are the speed and unite vector of the rigid-body velocity. Let β be the angle of the body's main axis with the horizontal plane, γ be the angle of the body's velocity \mathbf{u} with the horizontal plane, and α be the attack angle between the direction of the main body axis (\mathbf{e}) and the direction of the body velocity (\mathbf{e}_u)^[4] (Fig. 2),

$$\alpha = \cos^{-1}(\mathbf{e}_u \cdot \mathbf{e}), \quad \beta = \sin^{-1}(\mathbf{e} \cdot \mathbf{k}), \quad \gamma = \sin^{-1}(\mathbf{e}_u \cdot \mathbf{k}). \quad (4)$$

Usually, the unit vector \mathbf{e}_u is represented by (Fig. 3)

$$\mathbf{e}_u = \cos \gamma \cos \psi \mathbf{i} + \cos \gamma \sin \psi \mathbf{j} + \sin \gamma \mathbf{k}. \quad (5)$$

where ψ is the azimuth angle. Differentiation of (5) with respect to t gives

$$\frac{d\mathbf{e}_u}{dt} = \frac{d\gamma}{dt} \mathbf{e}_u^\gamma + \frac{d\psi}{dt} \cos \gamma \mathbf{e}_u^\psi, \quad (6)$$

where

$$\mathbf{e}_u^\psi = -\sin \psi \mathbf{i} + \cos \psi \mathbf{j}, \quad \mathbf{e}_u^\gamma = -\sin \gamma \cos \psi \mathbf{i} - \sin \gamma \sin \psi \mathbf{j} + \cos \gamma \mathbf{k}, \quad (7)$$

are unit vectors. It is clear that

$$\mathbf{e}_u^\psi \perp \mathbf{e}_u, \quad \mathbf{e}_u^\gamma \perp \mathbf{e}_u, \quad \mathbf{e}_u^\gamma \perp \mathbf{e}_u^\psi. \quad (8)$$

Let \mathbf{V}_w be the water velocity. Water-to-body relative velocity \mathbf{V} (called the relative velocity) is represented by

$$\mathbf{V} \equiv \mathbf{V}_w - \mathbf{u} \approx -\mathbf{u} = -U\mathbf{e}_u. \quad (9)$$

Here, the water velocity is assumed much smaller than the rigid-body velocity. A third basic unit vector (\mathbf{e}_m^h) can be defined perpendicular to both \mathbf{e} and \mathbf{e}_u ,

$$\mathbf{e}_m^h = \frac{\mathbf{e}_u \times \mathbf{e}}{|\mathbf{e}_u \times \mathbf{e}|}. \quad (10)$$

The drag force (\mathbf{F}_d) is in the opposite direction of the rigid-body velocity. The lift force (\mathbf{F}_l) is in the plane constructed by the two vectors (\mathbf{e} , \mathbf{e}_u) (i.e., perpendicular to \mathbf{e}_m^h) and perpendicular to \mathbf{e}_u , and therefore the lift force is in the direction of $\mathbf{e}_m^h \times \mathbf{e}_u$. Both drag and lift forces, exerting on the center of volume, are represented by

$$\mathbf{F}_d = -f_d \mathbf{e}_u, \quad \mathbf{F}_l = f_l \mathbf{e}_l, \quad \mathbf{e}_l = \mathbf{e}_m^h \times \mathbf{e}_u, \quad (11)$$

where f_d and f_l are the magnitudes of the forces. The magnitudes (f_d , f_l) are represented by the drag law^[5],

$$f_d = \frac{1}{2} C_d \rho A_w U^2, \quad f_l = \frac{1}{2} C_l \rho A_w U^2, \quad (12)$$

where ρ is water density; A_w is the under water projection area; (C_d , C_l) are the drag and lift coefficients, which are determined by the experiments.

Bomb is a fast moving rigid-body usually with four fins. Two fins in the same plane are called the pair of fins. For simplicity, these fins are treated approximately as the NACA0015 airfoils (Fig. 4) with known drag and lift coefficients. For example, they are listed at <http://www.aerospaceweb.org/question/airfoils/q0150b.shtml>. Using these coefficients, the combined drag and lift forces on a pair of fins (\mathbf{F}_c^f) can be calculated. If the bomb has n pairs of fins, the total drag and lift forces on the fins are represented by $n \mathbf{F}_c^f$.

2.2. Translation Torque

As the drag/lift forces are defined on the center of volume, the hydrodynamic torque (relative to center of mass) \mathbf{M}_h is caused by (a) drag and lift forces exerted on o_v to o_m , (b) moment of drag/lift forces exerted on o_v (\mathbf{M}_{tr}) and (c) anti-rotation of the rigid-body (\mathbf{M}_{rot}),

$$\mathbf{M}_h = -\sigma \mathbf{e} \times (\mathbf{F}_d + \mathbf{F}_l) - n \sigma_f \mathbf{e} \times \mathbf{F}_c^f + \mathbf{M}_{tr} + \mathbf{M}_{rot}. \quad (13)$$

The torque \mathbf{M}_{tr} is perpendicular to both \mathbf{e}_u (the direction of \mathbf{V}) and \mathbf{e} (the body orientation), and therefore it is in the same direction of the unit vector \mathbf{e}_m^h ,

$$\mathbf{M}_{tr} = M_{tr} \mathbf{e}_m^h, \quad (14)$$

where M_{tr} is the magnitude of the anti-translation torque, and be calculated by the drag law^[4],

$$M_{tr} = \frac{1}{2} C_m \rho A_w L_w U^2, \quad (15)$$

where C_m is the anti-translation torque coefficient.

2.3. Anti-Rotation Torque

The anti-rotation torque acts as the rigid-body rotates. Let $\mathbf{\Omega}^*$ be the rigid-body's angular velocity vector, which is decomposed into two parts with one along the unit vector \mathbf{e} (bank angle) and the other $\mathbf{\Omega}$ (azimuthal and elevation angles) perpendicular to \mathbf{e} (Fig. 5),

$$\mathbf{\Omega}^* = \Omega_s \mathbf{e} + \mathbf{\Omega}. \quad (16)$$

Let \mathbf{e}_ω be the unit vector in the direction of $\mathbf{\Omega}$,

$$\mathbf{\Omega} = \Omega \mathbf{e}_\omega, \quad \Omega = |\mathbf{\Omega}|. \quad (17)$$

The unit vector \mathbf{e}_ω is perpendicular to \mathbf{e} ,

$$\mathbf{e}_\omega \cdot \mathbf{e} = 0. \quad (18)$$

Time rate of change of the unit vector \mathbf{e} (main axis direction) is given by

$$\frac{d\mathbf{e}}{dt} = \boldsymbol{\Omega}^* \times \mathbf{e} = \boldsymbol{\Omega} \times \mathbf{e}. \quad (19)$$

Vector product between (19) and the unit vector \mathbf{e} gives

$$\mathbf{e} \times \frac{d\mathbf{e}}{dt} = \boldsymbol{\Omega} = \Omega \mathbf{e}_\omega. \quad (20)$$

Differentiation of (16) with respect to time t and use of (20) lead to^[6]

$$\frac{d\boldsymbol{\Omega}^*}{dt} = \frac{d\Omega_s}{dt} \mathbf{e} + \Omega_s (\boldsymbol{\Omega} \times \mathbf{e}) + \frac{d\boldsymbol{\Omega}}{dt}. \quad (21)$$

The anti-rotation torque (\mathbf{M}_{rot}) is against the rotation of the rigid body $\boldsymbol{\Omega}^*$. It can be decomposed into two parts,

$$\mathbf{M}_{rot} = \mathbf{M}_s + \mathbf{M}_c, \quad (22)$$

where the torque \mathbf{M}_s (resistant to self spinning, $\Omega_s \mathbf{e}$) parallels the main axis of the body (i.e., the unit vector \mathbf{e}),

$$\mathbf{M}_s = -M_s \mathbf{e}, \quad (23)$$

and the torque \mathbf{M}_c is perpendicular to the unit vector \mathbf{e} ,

$$\mathbf{M}_c = -M_c \mathbf{e}_\omega, \quad \mathbf{e}_\omega \perp \mathbf{e}, \quad (24)$$

where M_s and M_c are the corresponding scalar parts. The drag law shows that^[7]

$$M_s = \frac{1}{2} C_s \rho A_w L_w^3 |\Omega_s| \Omega_s, \quad (25)$$

$$M_c = \frac{1}{2} CF (\Omega L_w / V_r) \rho A_w L_w V_r^2. \quad (26)$$

where C_s is the torque coefficient for self-spinning; C is the drag coefficient due to cross-body flow. The function $F(\mu)$ is obtained from surface integration of torque due to cross-body hydrodynamic force (perpendicular to the body). For a cylindrical body, the coefficient C and function $F(\mu)$ are given by^{[8][9]}

$$C = \begin{cases} 1.9276 + 8/\text{Re}, & \text{if } \text{Re} \leq 12 \\ 1.261 + 16/\text{Re}, & \text{if } 12 < \text{Re} \leq 180 \\ 0.855 + 89/\text{Re}, & \text{if } 180 < \text{Re} \leq 2000 \\ 0.84 + 0.00003\text{Re}, & \text{if } 2000 < \text{Re} \leq 12000 \\ 1.2 - 4/\delta & \text{if } 12000 < \text{Re} \leq 150000, \delta \geq 10 \\ 0.835 - 0.35/\delta, & \text{if } 12000 < \text{Re} \leq 150000, 2 \leq \delta < 10 \\ 0.7 - 0.08/\delta, & \text{if } 12000 < \text{Re} \leq 150000, \delta < 2 \\ 1.875 - 0.0000045\text{Re}, & \text{if } 150000 < \text{Re} \leq 350000 \\ 1/(641550/\text{Re} + 1.5), & \text{if } \text{Re} > 350000. \end{cases} \quad (27)$$

$$F(\mu) \equiv \begin{cases} \frac{1}{6\mu}, & \text{for } \mu \geq 1/2 \\ \left[\left(\frac{1}{4} - \mu^2 \right) + \frac{4}{3}\mu^2 + \frac{1}{2\mu^2} \left(\frac{1}{16} - \mu^4 \right) \right], & \text{for } \mu < 1/2 \end{cases} \quad (28)$$

Here, δ is the aspect ratio of the rigid body; $\text{Re} = UD/\nu$, is the Reynolds number with D the effective diameter of rigid body; V_r is the projection of the water-to-body relative velocity on the vector $\mathbf{e}_r = \mathbf{e}_\omega \times \mathbf{e}$,

$$V_r = \mathbf{V} \cdot \mathbf{e}_r = -U\mathbf{e}_u \cdot (\mathbf{e}_\omega \times \mathbf{e}), \quad (29)$$

where Eq.(9) is used. For a supercavitation area, a correction factor may be multiplied to the coefficient C .

3. Dynamics

3.1. Momentum Equation

Differentiation of (3) with respect to time t gives the acceleration of the rigid body,

$$\frac{d\mathbf{u}}{dt} = \frac{dU}{dt} \mathbf{e}_u + U \frac{d\mathbf{e}_u}{dt}. \quad (30)$$

The momentum equation in the earth-fixed coordinate system is given by (Fig. 3),

$$m \left(\frac{dU}{dt} \mathbf{e}_u + U \frac{d\mathbf{e}_u}{dt} \right) = \mathbf{F}. \quad (31)$$

where \mathbf{F} is the resultant force consisting of,

$$\mathbf{F} = \mathbf{F}_g + \mathbf{F}_b + \mathbf{F}_d + \mathbf{F}_l + n\mathbf{F}_c^f. \quad (32)$$

Here,

$$\mathbf{F}_g = -mg\mathbf{k}, \quad \mathbf{F}_b = \rho\Pi g\mathbf{k}, \quad (33)$$

are the gravity and buoyancy force and Π is the volume of the rigid body. For bomb without fin ($n = 0$), the resultant force is represented by

$$\mathbf{F} = \mathbf{F}_g + \mathbf{F}_b + \mathbf{F}_d + \mathbf{F}_l. \quad (34)$$

Inner products between Eq.(31) and the unit vectors $(\mathbf{e}_u, \mathbf{e}_u^\psi, \mathbf{e}_u^\gamma)$ for $n = 0$ lead to

$$m \frac{dU}{dt} = (\rho\Pi - m)g\mathbf{k} \cdot \mathbf{e}_u - f_d, \quad (35)$$

$$mU \frac{d\gamma}{dt} = [(\rho\Pi - m)g\mathbf{k} + f_l\mathbf{e}_l] \cdot \mathbf{e}_u^\gamma, \quad (36)$$

$$mU \cos\gamma \frac{d\psi}{dt} = [(\rho\Pi - m)g\mathbf{k} + f_l\mathbf{e}_l] \cdot \mathbf{e}_u^\psi. \quad (37)$$

Here, we use (8) and the condition $\mathbf{e}_l \perp \mathbf{e}_v$ (i.e., the lift force perpendicular to the drag force). The vector $[(\rho\Pi - m)g\mathbf{k} + f_l\mathbf{e}_l]$ in (36) and (37) can be represented by

$$[(\rho\Pi - m)g\mathbf{k} + f_l\mathbf{e}_l] = (m \frac{dU}{dt} + f_d)\mathbf{e}_u + mU \frac{d\gamma}{dt} \mathbf{e}_u^\gamma + mU \cos\gamma \frac{d\psi}{dt} \mathbf{e}_u^\psi, \quad (38)$$

which shows that this vector has the component of $(mdU/dt + f_d)$ in the direction of \mathbf{e}_u , $mU d\gamma/dt$ in the direction of \mathbf{e}_u^γ , and $mU \cos \gamma d\psi/dt$ in the direction of \mathbf{e}_u^ψ . Inner product of (38) by the unit vector \mathbf{e}_l leads to

$$\left[(-m + \rho\Pi)g\mathbf{k} + f_l\mathbf{e}_l\right] \cdot \mathbf{e}_l = \left[mU \frac{d\gamma}{dt} \mathbf{e}_u^\gamma + mU \cos \gamma \frac{d\psi}{dt} \mathbf{e}_u^\psi \right] \cdot \mathbf{e}_l, \quad (39)$$

where the condition $(\mathbf{e}_u \perp \mathbf{e}_l)$ is used [see (11)].

3.2. Moment of Momentum Equation

The moment of momentum equation (relative to center of mass) is given by

$$\mathbf{J} \cdot \frac{d\boldsymbol{\Omega}^*}{dt} = \mathbf{M}_b + \mathbf{M}_h, \quad (40)$$

where

$$\mathbf{M}_b = -\sigma \mathbf{e} \times (\rho\Pi g \mathbf{k}), \quad (41)$$

is the torque caused by buoyancy force (called the buoyancy torque). \mathbf{J} is gyration tensor.

In the body-fixed coordinate system \mathbf{J} is a diagonal matrix [7]

$$\mathbf{J} = \begin{bmatrix} J_1 & 0 & 0 \\ 0 & J_2 & 0 \\ 0 & 0 & J_3 \end{bmatrix}, \quad (42)$$

with J_1 , J_2 , and J_3 are the moments of inertial. For axially symmetric rigid-body such as bomb, $J_2 = J_3$. Substitution of (13) into (40) and use of (11) and (22) lead to

$$\mathbf{J} \cdot \frac{d\boldsymbol{\Omega}^*}{dt} = \mathbf{M}_s + \hat{\mathbf{M}}, \quad (43)$$

where

$$\hat{\mathbf{M}} \equiv -\sigma\rho\Pi g \mathbf{e} \times \mathbf{k} - \sigma(f_d \mathbf{e} \times \mathbf{e}_u + f_l \mathbf{e} \times \mathbf{e}_l) - n\sigma_f f_c^f \mathbf{e} \times \mathbf{e}_c^f + \mathbf{M}_{tr} + \mathbf{M}_c. \quad (44)$$

Since \mathbf{M}_s is the anti-self-spinning torque which parallels the unit vector \mathbf{e} , and $\hat{\mathbf{M}}$ is the torque perpendicular to the unit vector \mathbf{e} , the moment of momentum equation (43) can be decomposed into two components with one parallel to \mathbf{e} ^[10],

$$J_1 \frac{d\Omega_s}{dt} = -M_s, \quad (45)$$

and the other perpendicular to \mathbf{e} ,

$$\frac{d\mathbf{\Omega}}{dt} = \frac{\hat{\mathbf{M}}}{J_2} - \Omega_s (\mathbf{\Omega} \times \mathbf{e}), \quad (46)$$

where (24) is used. For a rigid-body with very slow or no self spinning (such as bomb), $\Omega_s \approx 0$, Eq.(46) becomes

$$J_2 \frac{d\mathbf{\Omega}}{dt} = \hat{\mathbf{M}}. \quad (47)$$

4. Diagnostic Relationships

The momentum equations (35) and (39) can be rewritten by

$$C_d = \frac{2[(\rho\Pi - m)g\mathbf{k} \cdot \mathbf{e}_u - mdU/dt]}{\rho A_w U^2}, \quad (48)$$

$$C_l = \frac{2[mU(\mathbf{e}_u^\gamma d\gamma/dt + \mathbf{e}_u^\psi \cos\gamma d\psi/dt) \cdot \mathbf{e}_l - (\rho\Pi - m)g\mathbf{k} \cdot \mathbf{e}_l]}{\rho A_w U^2}. \quad (49)$$

Inner products of (47) by the unit vectors \mathbf{e}_m^h (direction of \mathbf{M}_{tr}) for without fin ($n = 0$) and \mathbf{e}_ω (direction of \mathbf{M}_{ae}) lead to

$$\begin{aligned} C_m = & \frac{J_2 \frac{d\mathbf{\Omega}}{dt} \cdot \mathbf{e}_m^h + \sigma\rho\Pi g(\mathbf{e} \times \mathbf{k}) \cdot \mathbf{e}_m^h}{\frac{1}{2}\rho A_w L_w U^2} + CF(\Omega L_w/V_r) \frac{V_r^2}{U^2} \mathbf{e}_\omega \cdot \mathbf{e}_m^h \\ & + \frac{\sigma}{L_w} [C_d(\mathbf{e} \times \mathbf{e}_u) \cdot \mathbf{e}_m^h + C_l(\mathbf{e} \times \mathbf{e}_l) \cdot \mathbf{e}_m^h], \end{aligned} \quad (50)$$

Eqs.(48)-(50) are the diagnostic relationships for determining the coefficients (C_d , C_l , C_m). In the righthand sides of (48)-(50), the unit vectors (\mathbf{e} , \mathbf{e}_v , \mathbf{e}_ω) are essential, and the other unit vectors (\mathbf{e}_l , \mathbf{e}_m^h , \mathbf{e}_u^w , \mathbf{e}_u^γ) are derived.

Accurate prediction of a high-speed rigid body's location and orientation in the water column needs realistic values of the drag/lift and torque coefficients (C_d , C_l , C_m). Among these coefficients, (C_d , C_l , C_m) depend on the attack angle (α).

Effects of special phenomena such as surface impact, bubbles, and supercavitation on the movement of rigid body are represented in the change of these coefficients. Thus, if the time evolutions of unit vectors (\mathbf{e} , \mathbf{e}_u , \mathbf{e}_ω) and variables (x, y, z, U, ψ, χ) are measured, time evolutions of the drag/lift and torque coefficients (C_d , C_l , C_m) can be obtained using the diagnostic relationships (48)-(50). The rotation rate Ω is calculated from the time series of (ψ, χ).

With large-amount of derived (C_d , C_l , C_m) data, instantaneous relationships (semi-empirical formulas) can be established statistically between (C_d , C_l , C_m) and basic parameters such as the attack angle α , Reynolds number (Re), and the rotation rate Ω . A traditional method for this purpose is to conduct experiments in the wind tunnel. Use of wind tunnel may be feasible for determining the drag/lift and torque coefficients of a rigid body in the air, but not realistic in the water especially the rigid body with high speed such as bomb.

5. Photographic Method

5.1. General Description

As alternative to the wind tunnel method, the photographic method is used to measure time evolutions of rigid-body's head and tail points $\mathbf{r}_h(t)$ and $\mathbf{r}_t(t)$ using HSV

cameras ^[11]. From the $[\mathbf{r}_h(t), \mathbf{r}_t(t)]$ data, the time series of the unit vectors (\mathbf{e} , \mathbf{e}_u , \mathbf{e}_ω), variables (x, y, z, U, ψ, χ), and attack angle (α) can be calculated using (3), (4), (5), and (23). With the diagnostic relationships (48)-(50), time evolutions of the drag/lift and torque coefficients (C_d , C_l , C_m) can be obtained.

5.2. Model Design and Construction

Details of the full-scale Mk84 with a guidance tail section were obtained from Boeing Corporation with the mass inertia properties for the complete Mk84 warhead and tail section as well as for the modifications to the tail section including removal of two fins, four fins, and the complete tail section. We developed a closed form analytical model to determine the outer casing material and thickness and type of internal components and their location for the 1/12-scale model to match the scaled total mass, center of gravity and radius of gyration values for the Mk84 bomb with the different tail configurations. Here, the overall outer shape of the scaled Mk84 bomb represented an exact dimensional replica of the full-scale system. Fig. 6 shows the overall design details of each model configuration. The outer casing was made from 7075-T6 aluminum. For the models with a tail section, the casing was fabricated in two pieces that were screwed together near the center point. To obtain the correct mass properties, a copper plug was inserted inside the model and then the remaining internal cavity was filled with a low density Epoxy. For all of the models with a tail section, only small differences in the copper plug size was required to match the mass properties. For these models the Epoxy had a density of 0.546 kg m^{-3} . For the model with no tail section, two copper plugs were required and the Epoxy density had to be increased to 1.168 kg m^{-3} by adding Tungsten

powder. Four types of model Mk-84 bombs were constructed: Type-I (tail with 4 fins), Type-II (tail with two fins), Type-III (tail with no fins), and Type-IV (no tail).

5.3. Experiment Procedure

Two experiments were conducted to demonstrate the feasibility of this method with 1/12th scale model of the general purpose bomb (Mk-84) as the fast moving rigid body. The first experiment was conducted at the Monterey Bay Aquarium Research Institute (MBARI) Unmanned Underwater Vehicle Test Tank (9.14 m × 13.72 m × 9.14 m) filled with standard sea water^{[12][13]}. The second experiment was conducted at a 6 m deep by 9 m diameter pool, located at the SRI's Corral Hollow Experiment Site^[14]. A pneumatic launcher (gas gun) was used to shoot the 1/12th model Mk-84 bomb into the water tank in the first (second) experiment with velocities up to 100 m s⁻¹ (454 m s⁻¹) (Fig. 7). Since the implementation is very similar between the two experiments and the second experiment has much larger speed, the second experiment is presented here to illustrate the photographic method.

Models of Mk-84 bombs with and without tail section are taken as examples to illustrate the methodology for determination of the drag/lift and torque coefficients (C_d , C_l , C_m), and in turn the prediction of location and orientation of a fast-moving rigid-body through the water column. The primary objective is to determine the Mk84 trajectory through the very shallow water zone to provide an estimate of the maximum bomb-to-target standoff and required fuse delay time for optimum target lethality. Because it is possible that a portion, or all, of the guidance tail section may become separated from the warhead during water entry, it is necessary to determine the Mk84 trajectory for a variety

of different tail configurations ranging from a warhead with a completely intact tail section and four fins to a warhead with the tail section completely.

Using the Hopkinson scaling laws, 1/12-scale Mk84 bomb models were designed and constructed in SRI that matched the overall casing shape and mass inertial properties of the full-scale Mk84 prototype. To model the different possible damaged tail configurations, we fabricated models that consisted of the warhead section with a complete tail section and four fins, a complete tail section and two fins, a complete tail section and no fins, and with the tail section removed.

The gas gun (0.10 m diameter and 1.52 m long) barrel was evacuated before launching the scale model to prevent an air blast from disturbing the water surface prior to the model impacting the water surface. At the end of the gas gun there was a massive steel ring to strip the sabot from the scale model. At high velocities there is some deviation from the theoretical calibration curve, which may be attributed to gas blow by around the sabot or friction. For the maximum gun operating pressure of 2,500 psi, we were able to achieve a nominal water-entry velocity of about 305 m s^{-1} .

Two orthogonal periscope housings were positioned in the pool to allow simultaneous above-water and below-water visualization of the model trajectory. The housings supported Phantom-7 HSV cameras, which were run at 10,000 fps. Five high-intensity, short duration (30 ms) flash bulbs were used to front-light the scale model as it entered the water and traveled under water. The HSV cameras and flash bulbs were triggered at the time the sabot was released within the gun.

5.4. Data Collection

For the complete Mk84 bomb system, including the warhead with tail section and 4 fins (Type-I), tail section and 2 fins (Type-II), tail section and no fin (Type-III), and no tail section (Type-IV) were launched at different nominal water-entry velocity regimes from 119.48 m s^{-1} to 308.83 m s^{-1} . Table 1 summarizes the overall experimental matrix and water-entry conditions. Typically, the water-impact angle of entry was between 88° and 90° . In Launches 10, 11, and 12 the sabot failed to fully support the scale model within the gun during the launch phase, resulting in the scale model impacting the sabot stripper plate before impacting the water. Sequences of images from the two orthogonal HSV cameras were generated for each launch (Fig. 8).

Therefore, 16 time series of the unit vectors $(\mathbf{e}, \mathbf{e}_u, \mathbf{e}_\omega)$, variables $(x, y, z, U, \psi, \chi, \boldsymbol{\Omega})$, and attack angle (α) were obtained for the four types of the model Mk-84 bombs. All the experimental data have been converted to full-scale values. We divided the 16 time series into two groups: (a) Launches 13, 14, 15 (called the working data) for determining semi-empirical formulas for the drag/lift and torque coefficients (C_d, C_l, C_m) , and (b) rest of the data for evaluating the semi-empirical formulas (called evaluation data).

6. Semi-Empirical Formulas

Statistical analysis was conducted on the working dataset (Type-IV: Launch-13, -14, and -15) at each time step (remember the data rate is 10,000 Hz) between (C_d, C_l, C_m) and $(\text{Re}, \alpha, \Omega)$. Following semi-empirical formulas have been established,

$$C_d = 0.02 + 0.35e^{-2\left(\alpha - \frac{\pi}{2}\right)^2} \left(\frac{\text{Re}}{\text{Re}^*}\right)^{0.2} + 0.008\Omega \sin \theta, \quad (51) \quad (53)$$

$$C_l = \begin{cases} 0.35 \sin(\theta_1) \left(\frac{\text{Re}}{\text{Re}^*} \right)^{0.2} & \text{if } \alpha \leq \frac{\pi}{2} \\ 0.1 \sin(\theta_2) - 0.015 \Omega \left(\frac{\text{Re}}{\text{Re}^*} \right)^2 \sin(\theta_2^{0.85}) & \text{if } \alpha > \frac{\pi}{2} \end{cases} \quad (52) \quad (54)$$

$$C_m = \begin{cases} 0.07 \sin(2\alpha) \left(\frac{\text{Re}^*}{\text{Re}} \right)^{0.2} & \text{if } \alpha \leq \frac{\pi}{2} \\ 0.02 \sin(2\alpha) \sqrt{\left(\frac{\text{Re}}{\text{Re}^*} \right)} & \text{if } \alpha > \frac{\pi}{2} \end{cases} \quad (53) \quad (55)$$

Here, $\text{Re}^* = 1.8 \times 10^7$, is the critical Reynolds number, and

$$\theta \equiv \left(\pi^{2.2} - (\pi - |\pi - 2\alpha|)^{2.2} \right)^{\frac{1}{2.2}} \text{sign}(\pi - 2\alpha), \quad (54) \quad (56)$$

$$\theta_1 = \pi \left(\frac{2\alpha}{\pi} \right)^{1.8}, \quad \theta_2 = 2\pi \left(\frac{2\alpha}{\pi} - 1 \right)^{0.7}. \quad (55) \quad (57)$$

The semi-empirical formulas (51)-(53) show that the drag/lift coefficients (C_d , C_l) depend more on (Re, α) and less on the rotation rate Ω . For the same attack angle (α), C_d increases with Re . For the same Re , C_d increases with α monotonically from 0° to 90° and reduces monotonically with α from 90° to 180° with a maximum value for $\alpha = 90^\circ$ (Fig. 9). The dependence of lift coefficient C_l on (Re, α) is a little complicated than C_d , especially for the attack angle larger than 90° (Fig. 10). The torque coefficient C_m depends only on (Re, α) (Fig. 11).

The momentum equations (35)-(37) and the moment of momentum equation (47) were integrated using the same parameters (such as the density ratio, length, radius, the center of volume, and the center of mass) and the drop initial conditions (speed and orientation) as in Type-III (tail without fin) and Type-IV (no tail) (see Table 1) after using (51)-(53) for (C_d, C_l, C_m) . The validity of the semi-empirical formulas (51)-(53)

are verified through comparison between calculated and observed bomb trajectories, orientations, and velocities.

7. Results and Verification

7.1. Type-I

This type is for the complete Mk84 bomb system, including the warhead with tail section and four fins. Seven launches (Launch-1 to Launch-7) were conducted at different nominal water-entry velocity regimes (119 ms^{-1} to 302 ms^{-1}). Fig. 8 shows a sequence of images from the two orthogonal HSV cameras for a nominal velocity of 295 ms^{-1} (Launch-3). The cavitating column generated by the Mk84 bomb motion consists of a tapered cone that has a maximum full scale diameter at the end of the tail section of about 0.9 m. This is about a factor of two larger than the maximum bomb diameter of 0.45 m. This cavity shape was about the same for all of the initial water-entry velocities between 119 ms^{-1} and 302 ms^{-1} .

Fig. 12 shows the comparison of bomb's translation and orientation for Type-I (Launch-1 to Launch-7) between the calculated and observed data. Both calculated and observed trajectories show similar patterns. For the low velocity regime of about 125 ms^{-1} (Launch-1 and Launch-7), at a full scale depth of 12 m, the horizontal position ranged between 0.1 m (Launch-7, Fig. 12g) and 0.67 m (Launch-1, Fig. 12a). The bomb trajectories are quite stable without oscillation and tumbling no matter the water entry velocity is high or low.

7.2. Type-II

This type is for the modified Mk84 bomb system including the warhead with a tail section and two fins. Three launches (Launch-10, -11, -19) were conducted at an average

water-entry velocity of about 294 ms^{-1} . Fig. 13 shows a sequence of images (Launch-11) from the two orthogonal HSV cameras with a water entry-velocity of 290 ms^{-1} . The cavitated column generated by the bomb motion consists of a tapered cone that has a maximum full-scale diameter at the end of the tail section of about 0.9 m. This is about a factor of two larger than the maximum bomb diameter of 0.45 m. Thus, the initial cavity shape was about the same as for the model with a tail section and four fins as described above.

Fig. 14 shows the comparison of bomb's translation and orientation for Type-II (Launch-10, -11, -19) between the calculated and observed data. Both calculated and observed trajectories show similar patterns. At full-scale depth of 12.2 m (i.e., 40 ft), the horizontal position ranged between 0.53 m (Launch-11) and 2.1 m (Launch-10). These values are about a factor of two larger than the values measured for Mk84 bomb configuration with a tail section and four fins. Also, there seems to be no correlation between trajectory path and initial impact angle. The removal of two fins causes the bomb to eventually make 180° turn and travel toward the surface. The 12.2 m depth is reached at about 45 ms after water entry.

7.3. Type-III

This type is for the modified Mk84 bomb system including the warhead with a tail section and no fin. Three launches (Launch-16, -17, -18) were conducted at an average water-entry velocity of about 298 ms^{-1} . Fig. 15 shows a sequence of images (Launch-17) from the two orthogonal HSV cameras with a water entry-velocity of 297 ms^{-1} . The cavitated column generated by the bomb motion consists of a tapered cone that has a maximum full-scale diameter at the end of the tail section of about 0.9 m. This is about a

factor of two larger than the maximum bomb diameter of 0.45 m. Thus, the initial cavity shape was about the same as for the model with a tail section and four fins and for the model with two fins as described above.

Fig. 16 shows the comparison of bomb's translation and orientation for Type-III (Launch-16, -17, -18) between the calculated and observed data. Both calculated and observed trajectories show similar patterns. At full-scale depth of 12.2 m (i.e., 40 ft), the horizontal position ranges between 2.1 m (Launch-18) and 3.5 m (Launch-17). These values are about a factor of 9.5 and 3.5, respectively, larger than the values measured for a Mk84 warhead with a tail section and four fins. Also, there seems to be no correlation between trajectory path and angle of impact. As shown in Figs. 15 and 16, the removal of four fins causes the bomb eventually to make 180° turn and travel toward the surface in a manner similar to the trajectory for a bomb with a tail section and two fins. The 12.2 m depth is reached at about 47 ms after water entry. In general, the model with a tail section and no fins shows a decrease in overall trajectory stability compared with a model with a tail section and two fins. This is evident primarily through larger horizontal positions.

7.4. Type-IV

This type is for the modified Mk84 bomb system including the warhead and no tail section. Three launches (Launch-13, -14, -15) were conducted at an average water-entry velocity of about 299 ms^{-1} . Fig. 17 shows a sequence of images (Launch-13) from the two orthogonal HSV cameras with a water entry-velocity of 297 ms^{-1} . The cavitating column generated by the bomb motion consists of a tapered cone that has a maximum full-scale diameter at the end of the tail section of about 0.9 m. This is about a factor of two larger than the maximum bomb diameter of 0.45 m. Thus, the initial cavity shape

was about the same as for the model with a tail section (four, two, and no fins) as described above.

Fig. 18 shows the comparison of bomb's translation and orientation for Type-IV (Launch-13, -14, -15) between the calculated and observed data. Both calculated and observed trajectories show similar patterns. At full-scale depth of 12.2 m (i.e., 40 ft), the bomb has rotated 180° such that the bomb is moving tail first. When the nose reaches a depth of 12.2 m, the nose horizontal position is between 5.5 m to 7.2 m. Launch-13 had a deviation of 4.3° from the vertical water entry angle, which was the largest deviation in all of the launches. However, comparison of the trajectories in Launch-13 and Launch-14, in which a 90° water-entry angle was obtained, indicates that there is no correlation between impact angle and trajectory path. Thus, the trajectory motion is dominated by instability of the bomb within the cavitating region. Different from the Mk-84 bomb with a tail section and no fin (or two fins), the Type-IV bombs are never moving up toward the surface (Fig. 18).

Figs. 19-21 show the comparison between predicted and observed time evolutions of the horizontal deviation (x) and depth position (z) of o_m , bomb speed (U), and angles (α, β, γ). The predicted values of these variables are consistent to the corresponding observed values. This confirms the validity of the semi-empirical formulas (53)-(55) for drag/lift and torque coefficients (C_d, C_l, C_m). The three launches show the same interesting results. The bomb nose reaches the 12.2 m depth at about 110 ms after water entry. At this depth the bomb nose velocity decreased by about 82%. The horizontal deviation (x) of o_m increases rapidly at first and then slowly with time, and about 6 m from the entry point as the bomb reached the depth of 12.2 m.

8. Tail Section Damage Effects

The experiments conducted with different tail configurations were performed to determine the effects on bomb trajectory for different possible postulated damage levels to the tail section. Because the tail section is comprised mostly of internal stiffeners with an external skin, it may be weaker than the warhead section and, therefore, may be damaged during initial water entry or during tail slap within the cavitated region. Fig. 22 shows the maximum measured trajectories for each tail configuration for a nominal water-entry velocity of about 297 ms^{-1} , i.e., Launch-2 (Type-I), Launch-19 (Type-II), Launch-17 (Type-III), and Launch-13 (Type-IV).

Table 2 summarizes data comparison of the overall trajectory behavior for the different tail configurations. For each trajectory parameter we show the value associated with a particular tail configuration and the percentage difference compared with a complete bomb having a tail section and four fins. The horizontal nose position significantly increases with increased levels of damage to the tail section. For a model with a tail section and two fins, no fins, and no tail section, the horizontal position values increase by 120%, 259%, and 575%, respectively. With regard to travel time at 12.2 m depth, only the no-tail configuration shows a significant increase of 179%.

9. Conclusions

(1) A new dynamic-photographic method has been developed to determine the drag/lift and torque coefficients (C_d , C_l , C_m) of a fast-moving rigid body in the water column. This method contains two parts: (1) establishment of the diagnostic relationship between (C_d , C_l , C_m) and the rigid-body's trajectory and orientation, and (2) data collection of trajectory and orientation of a fast moving rigid body using multiple high-

speed video cameras (10,000 Hz). Using the digital photographic data, semi-empirical formulas of (C_d , C_l , C_m) versus Reynolds number, attack angle, and rotation rate can be established. The cost of this method is much lower than the traditional method using the wind tunnel to determine (C_d , C_l , C_m).

(2) To demonstrate the feasibility and powerfulness of this method, an experiment was conducted with 1/12th scale model of the general purpose bomb (Mk-84) as the fast moving rigid body at a 6 m deep by 9 m diameter pool, located at the SRI's Corral Hollow Experiment Site. A gas gun was used to shoot the 1/12th model Mk-84 bomb into the water tank with velocities up to 304 ms⁻¹. Four types of Mk-84 model bombs were used with total 16 launches for the experiment: warhead with tail section and four fins (Type-1), with tail section and two fins (Type-1I), with tail section and no fin (Type-1II), and with no tail section (Type-IV). Among them, data from 3 launches in Type-IV were used to get the semi-empirical formulas for (C_d , C_l , C_m). The rest of data were used for verification.

(3) The momentum equations and moment of momentum equations were integrated with the same parameters (such as the density ratio, length, radius, the center of volume, and the center of mass) and the drop initial conditions (speed and orientation) as in the observations after using the semi-empirical formulas for (C_d , C_l , C_m). Consistent between calculated and observed bomb trajectories, orientations, and velocities show the powerfulness of this method.

(4) Both calculated (solving dynamic equations with the semi-empirical formulas) and experimental data show similar results. The cavitated column generated by the Mk84 bomb motion consists of a tapered cone that has a maximum full scale diameter at the end

of the tail section of about 0.9 m. This is about a factor of two larger than the maximum bomb diameter of 0.45 m. This cavity shape was about the same for all of the initial water-entry velocities and four types of model bombs.

(5) The horizontal nose position significantly increases with increased levels of damage to the tail section. For a model with a tail section and two fins, no fins, and no tail section, the horizontal position values increase by 120%, 259%, and 575%, respectively. With regard to travel time at 12.2 m (i.e., 40-ft) depth, only the no-tail configuration shows a significant increase of 179%.

(6) For bomb with a tail section and four fins, its trajectories are quite stable without oscillation and tumbling no matter the water entry velocity is high or low. Removal of two fins causes the bomb to eventually make 180° turn and travel toward the surface. Although having a similar trajectory pattern (i.e., making 180° turn and traveling toward the surface), the removal of four fins shows a decrease in overall trajectory stability compared with a model with a tail section and two fins. This is evident primarily through larger horizontal positions. For Mk-84 bomb without a tail section, the bomb has rotated 180° at full-scale depth of 12.2 m such that the bomb is moving tail first. Different from the Mk-84 bomb with a tail section and no fin (or two fins), the Mk-84 bombs without a tail section are never moving up toward the surface.

Acknowledgments

The Office of Naval Research Breaching Technology Program (Grant Number: N0001405WR20209) and Naval Oceanographic Office supported this study.

References

- [1] Chu, P.C., and C.W. Fan, 2006: Prediction of falling cylinder through air-water-sediment columns. *Journal of Applied Mechanics*, 73, 300-314.
- [2] Chu, P.C., and C.W. Fan, 2005: Pseudo-cylinder parameterization for mine impact burial prediction. *Journal of Fluids Engineering*, 127, 1515-152.
- [3] Chu, P.C., 2008: Mine impact burial prediction from one to three dimensions. *Applied Mechanics Reviews*, ASME Journal, in press.
- [4] Munson, B.R., and D.J. Cronin, 1998: Airfoils and wings. In “The Handbook of Fluid Dynamics”, edited by R. W. Johnson, CRC Press, 4-1 to 4-3.
- [5] Von Mises, R, 1959, *Theory of Flight*, 1st Ed., Dover Publications Inc., New York, 564-585 pp.
- [6] Chu, P.C., and C.W. Fan, 2007: Mine impact burial model (IMPACT35) verification and improvement using sediment bearing factor method. *IEEE Journal of Oceanic Engineering*, 32 (1), 34-48.
- [7] Chu, P.C., C.W. Fan, A. D. Evans, and A. Gilles, 2004: Triple coordinate transforms for prediction of falling cylinder through the water column. *Journal of Applied Mechanics*, 71, 292-298.
- [8] Rouse, H, 1938, *Fluid Mechanics for Hydraulic Engineers*, 1st Ed., McGraw-Hill Book Company Inc., New York, 422 pp.
- [9] Crowe, C.T., J.A. Roberson, and D.F. Elger, 2001, *Engineering Fluid Mechanics*. 7th Edition, John Wiley & Sons Inc, New York, 714 pp.
- [10] White, F. M., 1974, *Viscous Fluid Flow*, 1st Ed., McGraw-Hill Inc., New York, 712 pp.

- [11] Chu, P.C., A. Gilles, and C.W. Fan, 2005: Experiment of falling cylinder through the water column. *Experimental and Thermal Fluid Sciences*, 29, 555-568.
- [12] Chu, P.C., G. Ray, P. Fleischer, and P. Gefken, 2006: Development of three dimensional bomb maneuvering model, DVD-ROM (10 pages). Seventh Monterey International Symposium on Technology and Mine Problems, NPS, Monterey, California, May 1-4.
- [13] Ray, G., 2006: Bomb strike experiments for mine countermeasure. Master thesis in Meteorology and Oceanography, Naval Postgraduate School, Monterey, California, 197 pp.
- [14] Gefken, P.R., 2006: Evaluation of precision-guided bomb trajectory through water using scale-model experiments. SRI Final Technical Report – PYU-16600, 80 pp.

Table 1. Summary of Mk-84 underwater trajectory experimental matrix.

Launch Number	Model Type	Water-Entry Velocity (m/s)	Water-Entry Impact Angle (°)
1	I (tail with 4 fins)	132	89.2
2	I (tail with 4 fins)	297	90.0
3	I (tail with 4 fins)	295	88.8
4	I (tail with 4 fins)	302	88.5
5	I (tail with 4 fins)	227	88.0
6	I (tail with 4 fins)	219	89.0
7	I (tail with 4 fins)	119	88.2
8	II (tail with 2 fins)	impacted sabot	stripper plate
9	II (tail with 2 fins)	impacted sabot	stripper plate
10	II (tail with 2 fins)	295	90.0
11	II (tail with 2 fins)	290	90.0
12	II (tail with 2 fins)	impacted sabot	stripper plate
13	IV (no tail)	297	85.7
14	IV (no tail)	301	90.0
15	IV (no tail)	301	88.7
16	III (tail with no fin)	304	90.0
17	III (tail with no fin)	297	87.0
18	III (tail with no fin)	291	88.1
19	II (tail with 2 fins)	297	90.0

Table 2. Horizontal position shift and travel time at depth of 12.2 m (i.e., 40 ft) for Mk-84 warhead with different tail configurations.

Model Type	Horizontal Position Shift (Unit: m)	Travel Time (Unit: ms)
Tail with 4 Fins	0.96	46.2
Tail with 2 Fins	2.12	46.2
Tail with Non Fins	3.46	49.8
No Tail	6.50	129.5

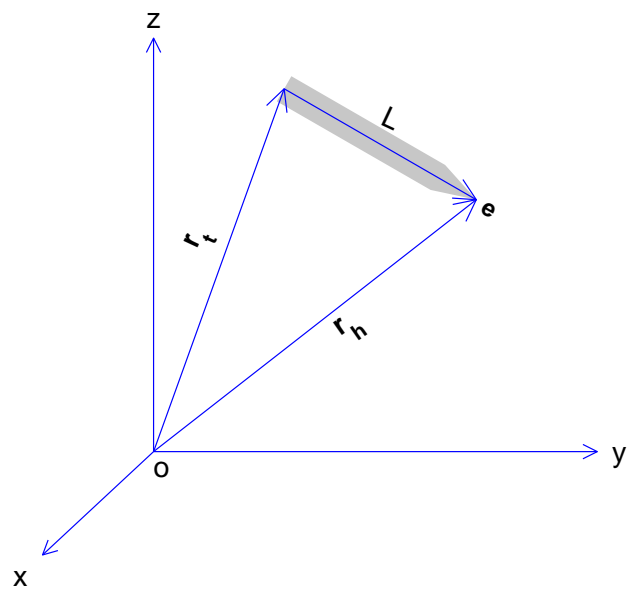


Fig. 1. Position vectors \mathbf{r}_h , \mathbf{r}_t , and the unit vector \mathbf{e} .

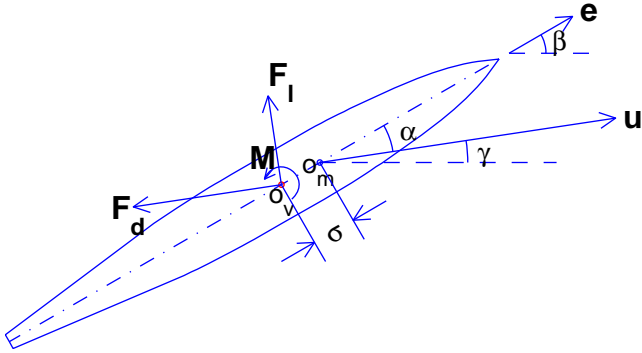


Fig. 2. Attack angle (α), angles (β, γ), center of volume (o_v), center of mass (o_m), and drag and lift forces (exerted on o_v). Note that σ is distance between o_v and o_m with positive (negative) value when the direction from o_v to o_m is the same (opposite) as the unit vector e .

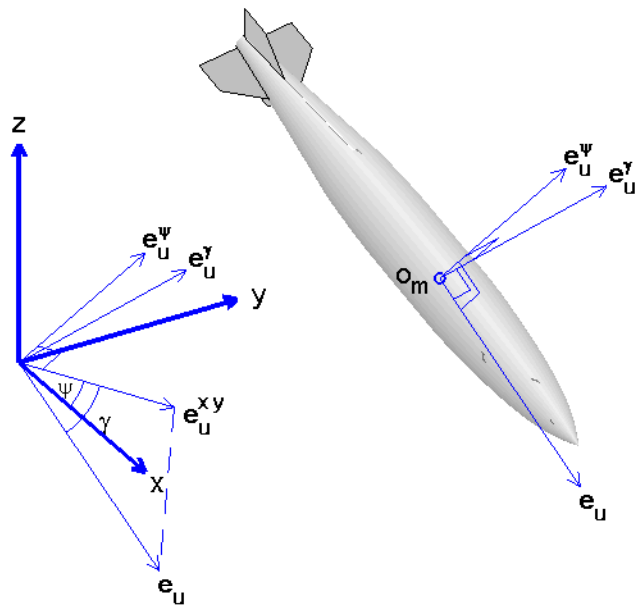


Fig. 3. Illustration of unit vectors (\mathbf{e}_u , \mathbf{e}_u^{ψ} , \mathbf{e}_u^{γ} , \mathbf{e}_u^{xy}) with \mathbf{e}_u^{xy} the projection of \mathbf{e}_u on the x - y plane.

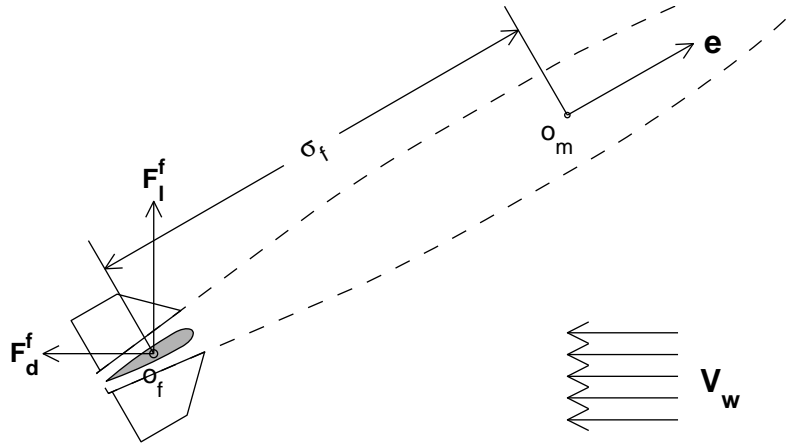


Fig. 4. Axial and cross-axial velocity (\mathbf{u}_a^f , \mathbf{u}_c^f), associated hydrodynamic forces on a pair of fins (\mathbf{F}_a^f , \mathbf{F}_c^f) and the distance between o_f and o_m (i.e., σ_f) with positive (negative) value when the direction from o_f to o_m is the same (opposite) as the unit vector \mathbf{e} .

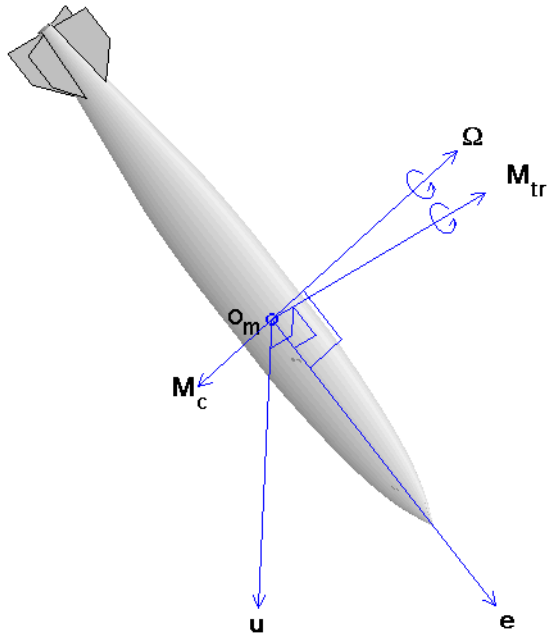


Fig. 5. Illustration of Ω , M_{tr} , M_c .

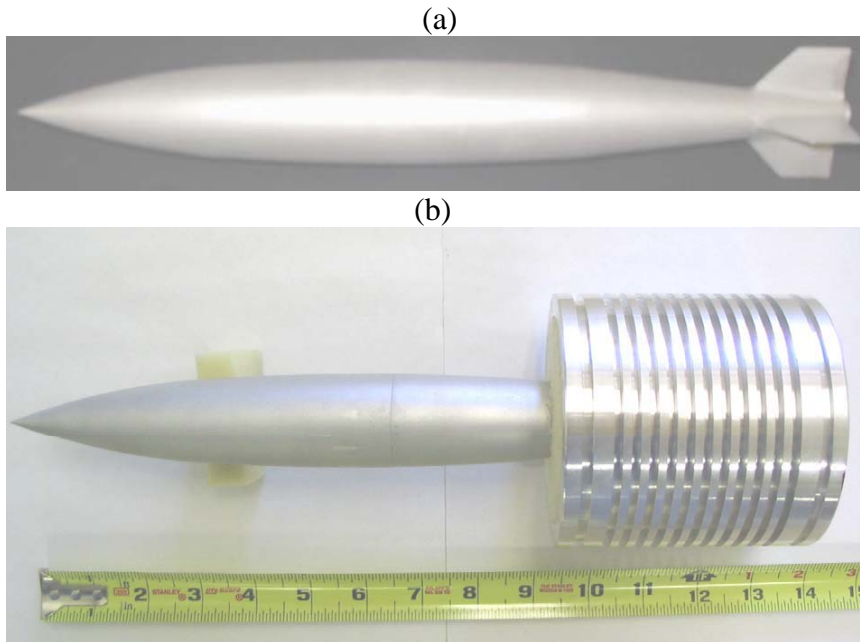


Fig. 6. Photography of $1/12^{\text{th}}$ scale model Mk-84 bomb: (a) warhead with tail section and four fins, and (b) sabot.



Fig. 7. Overview experimental arrangement.

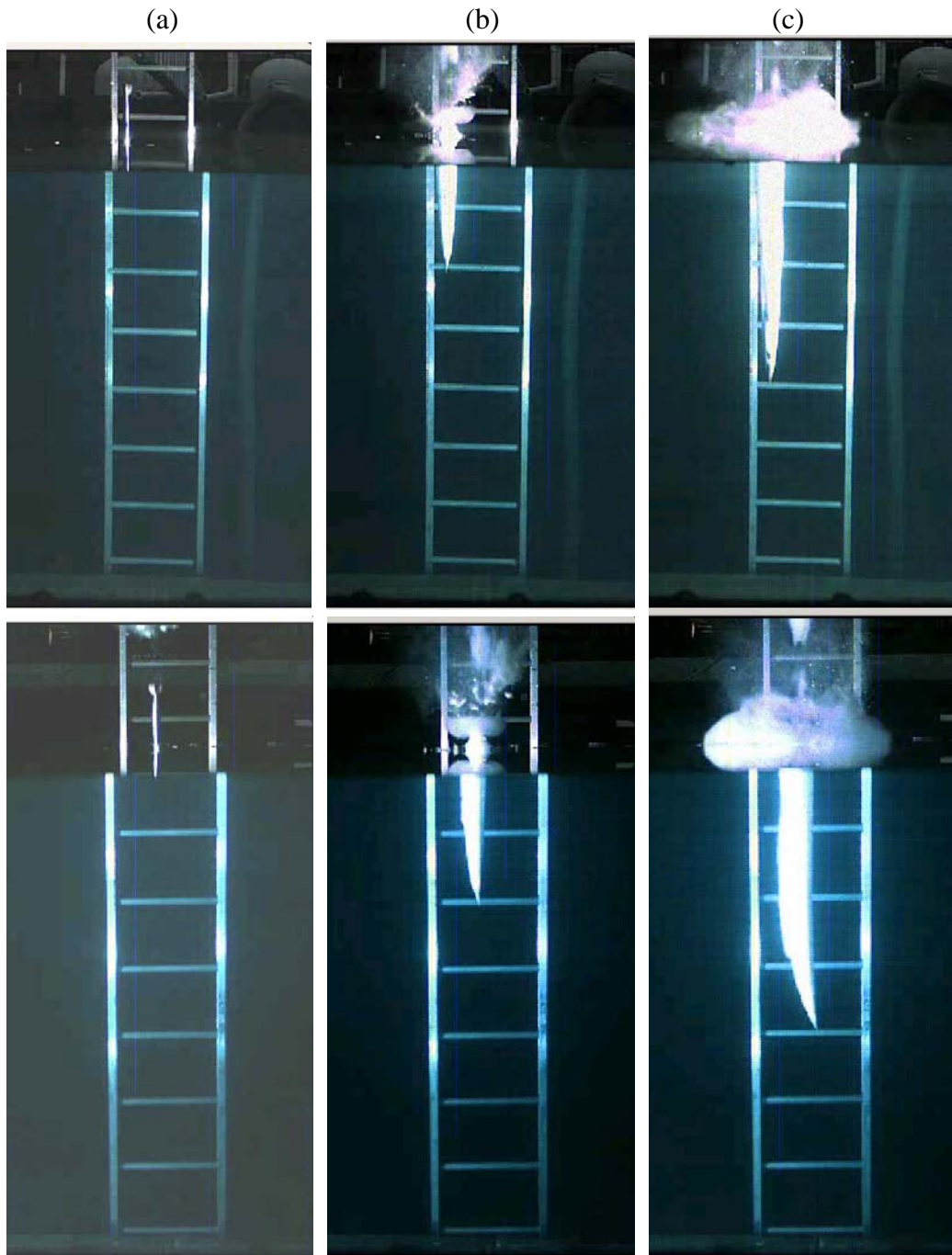


Fig. 8. Two HSV images for Launch-3 (Type-I) at water entry velocity of 295 ms^{-1} : initial water entry, (b) $t = 22.8$ ms, and (c) $t = 44.4$ ms.

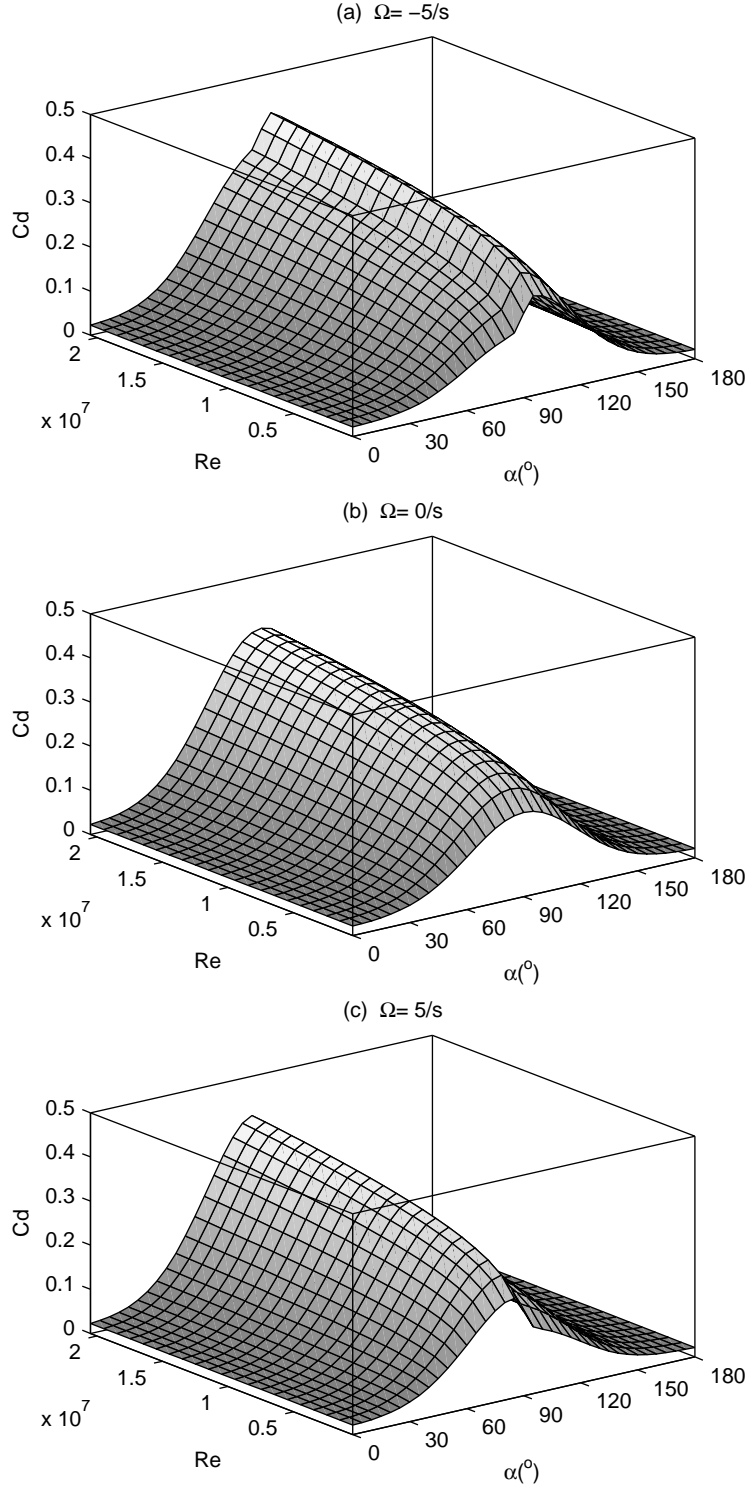


Fig. 9. Dependence of C_d on the Reynolds number (Re) and attack angle (α) for three different values of Ω : (a) -5 s^{-1} , (b) 0 , and (c) 5 s^{-1} .

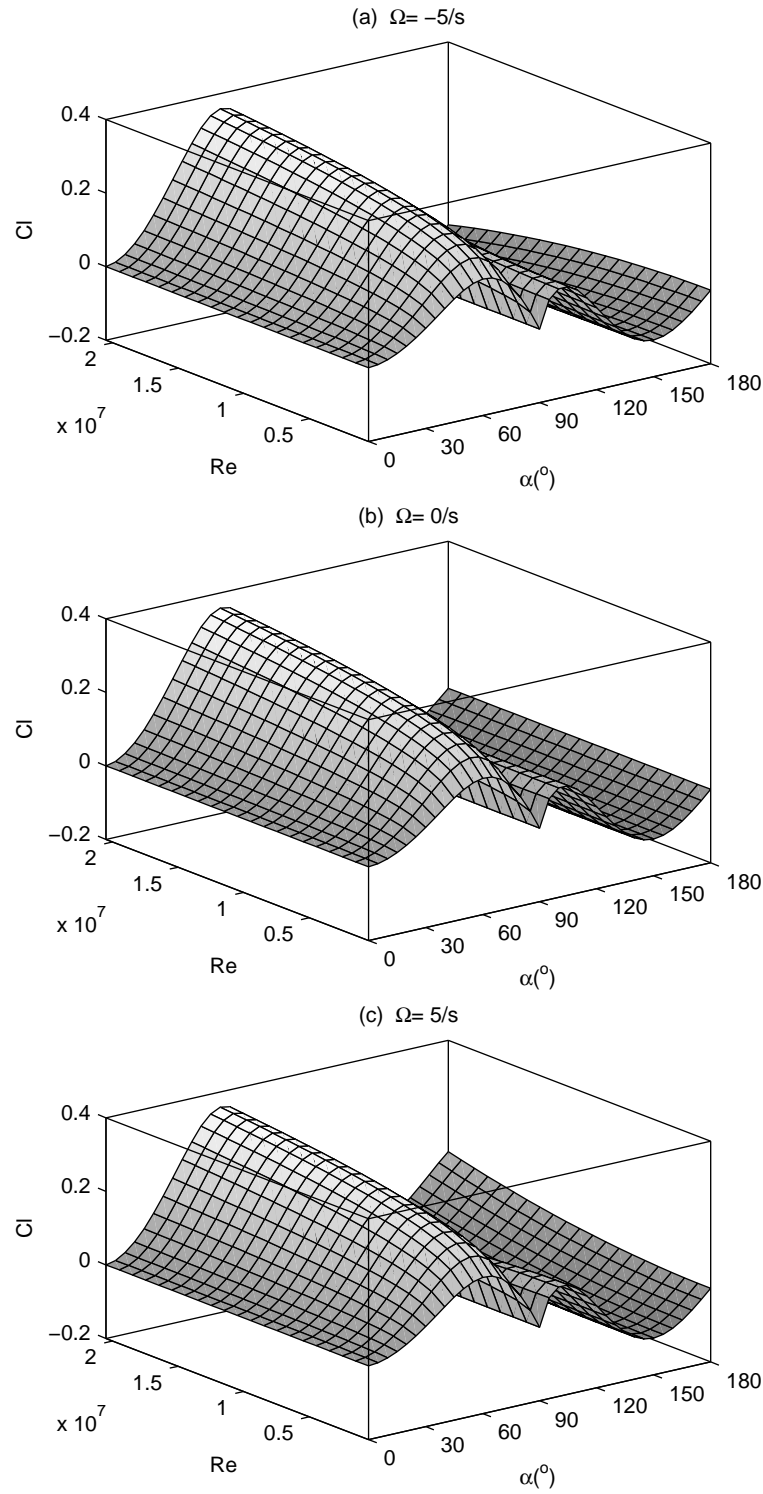


Fig. 10. Dependence of C_l on the Reynolds number (Re) and attack angle (α) for three different values of Ω : (a) -5 s^{-1} , (b) 0 , and (c) 5 s^{-1} .

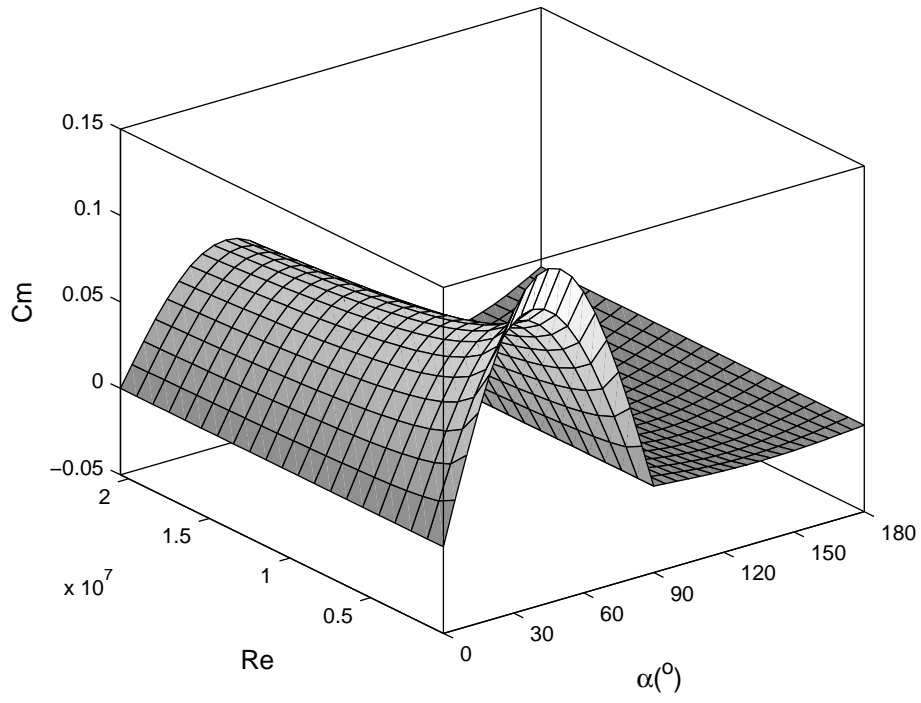


Fig. 11. Dependence of C_m on the Reynolds number (Re) and attack angle (α).

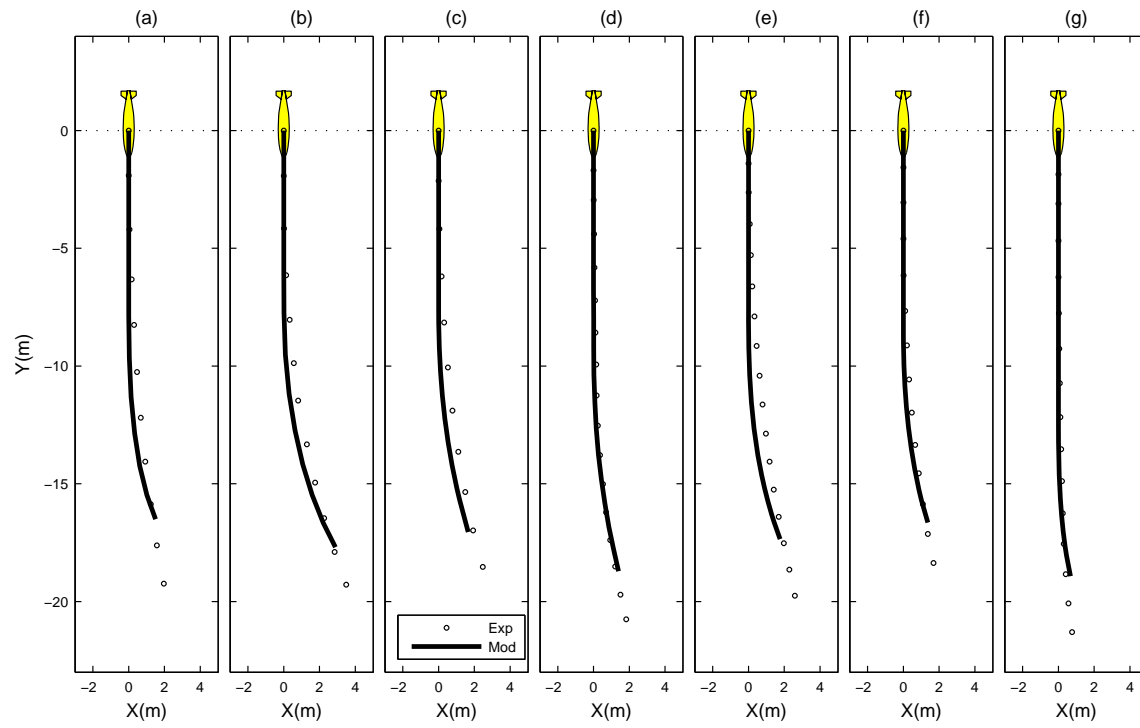


Fig. 12. Comparison between predicted and observed trajectories for Mk84 warhead with tail section and four fins (Type-1) with initial water entry speed: (a) 132 ms^{-1} , (b) 297 ms^{-1} , (c) 295 ms^{-1} , (d) 302 ms^{-1} , (e) 227 ms^{-1} , (f) 219 ms^{-1} , and (g) 119 ms^{-1} .

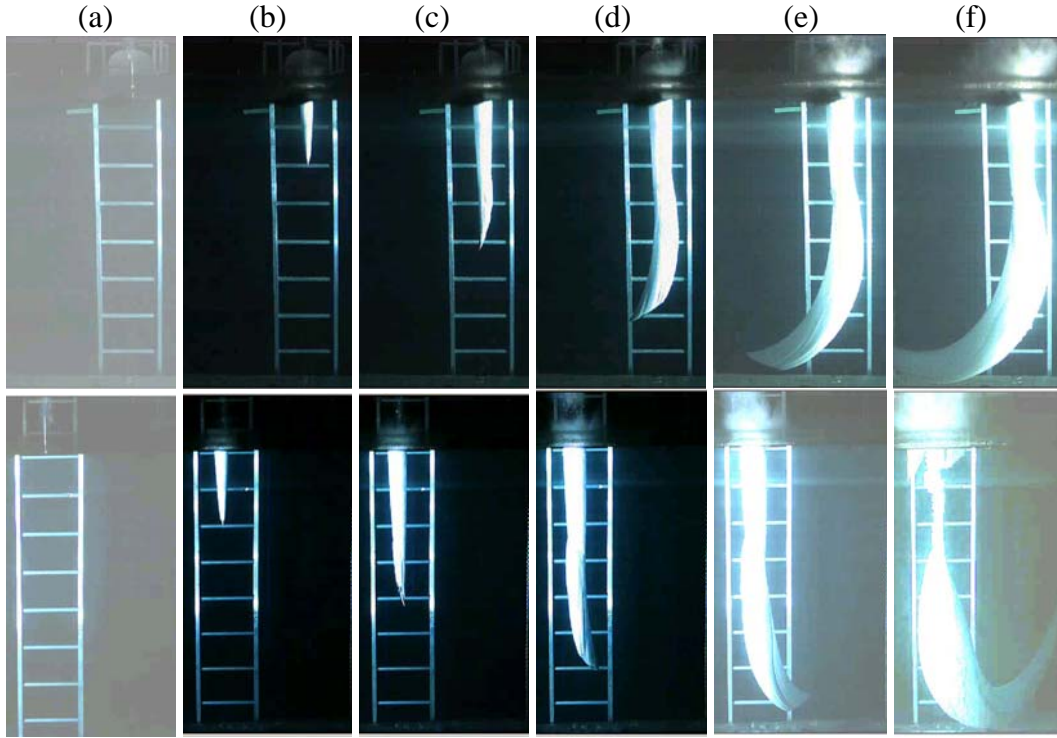


Fig. 13. Two HSV images for Launch-11 (Type-II) at water entry velocity of 290 ms^{-1} : (a) initial water entry, (b) $t = 21.6 \text{ ms}$, (c) $t = 48.0 \text{ ms}$, (d) $t = 75.6 \text{ ms}$, (e) $t = 116.4 \text{ ms}$, and (f) $t = 344.4 \text{ ms}$.

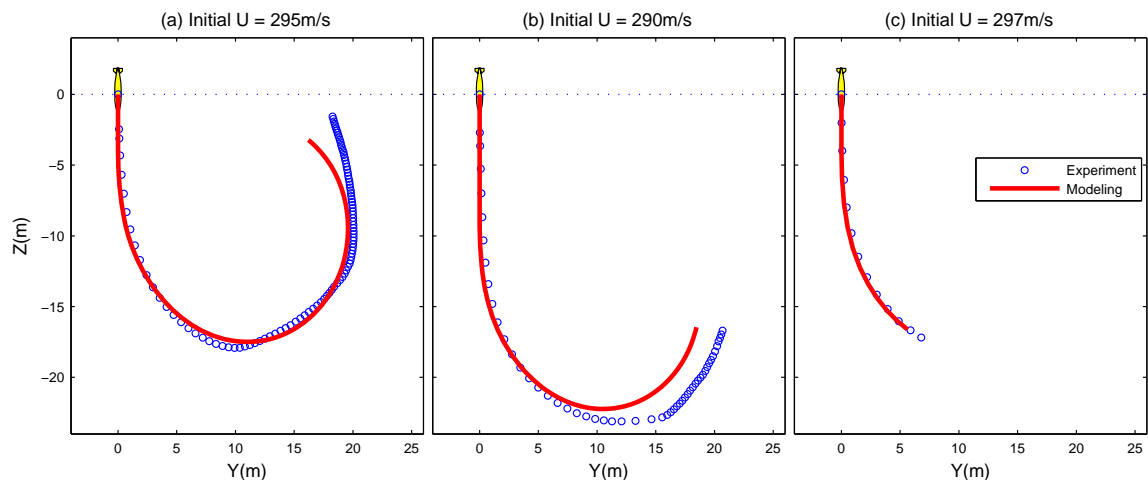


Fig. 14. Comparison between predicted and observed trajectories for Mk84 warhead with tail section and two fins (Type-1I) with initial water entry speed: (a) 295 ms^{-1} , (b) 290 ms^{-1} , and (c) 297 ms^{-1} .

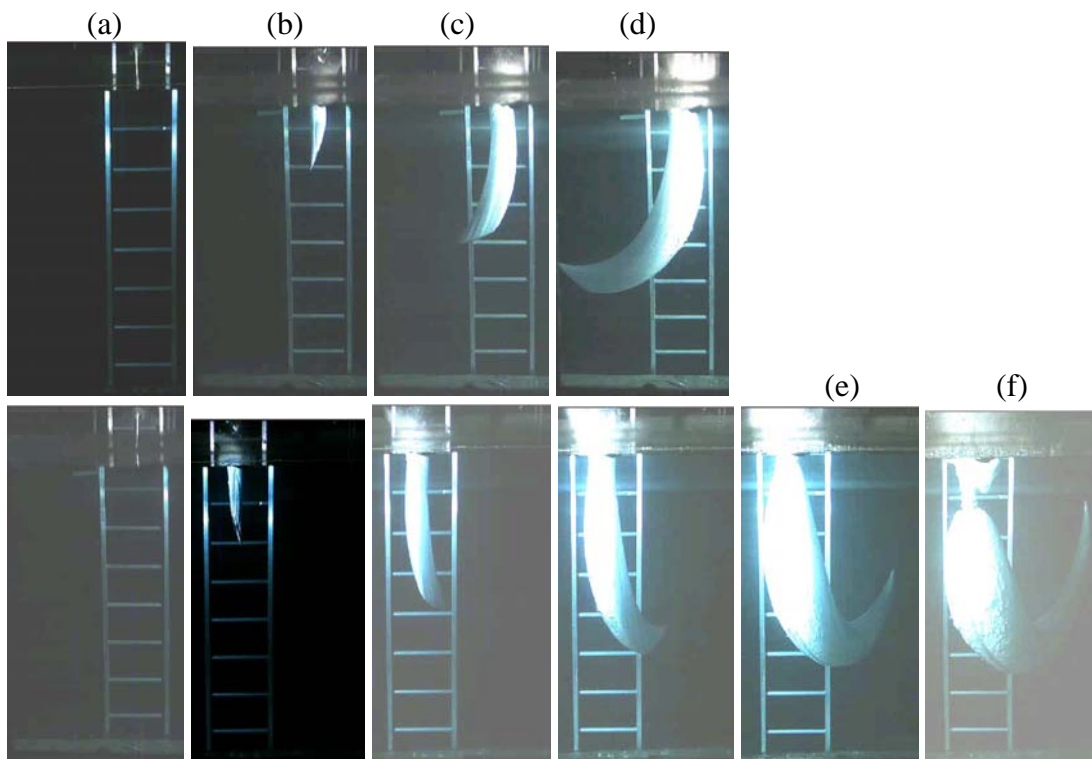


Fig. 15. Two HSV images for Launch-17 (Type-III) at water entry velocity of 298 ms^{-1} : (a) initial water entry, (b) $t = 22.8 \text{ ms}$, (c) $t = 55.2 \text{ ms}$, (d) $t = 99.0 \text{ ms}$, (e) $t = 211.2 \text{ ms}$, and (f) $t = 376.2 \text{ ms}$. Note that for time longer than 99.0 ms , only one HSV camera got the pictures.

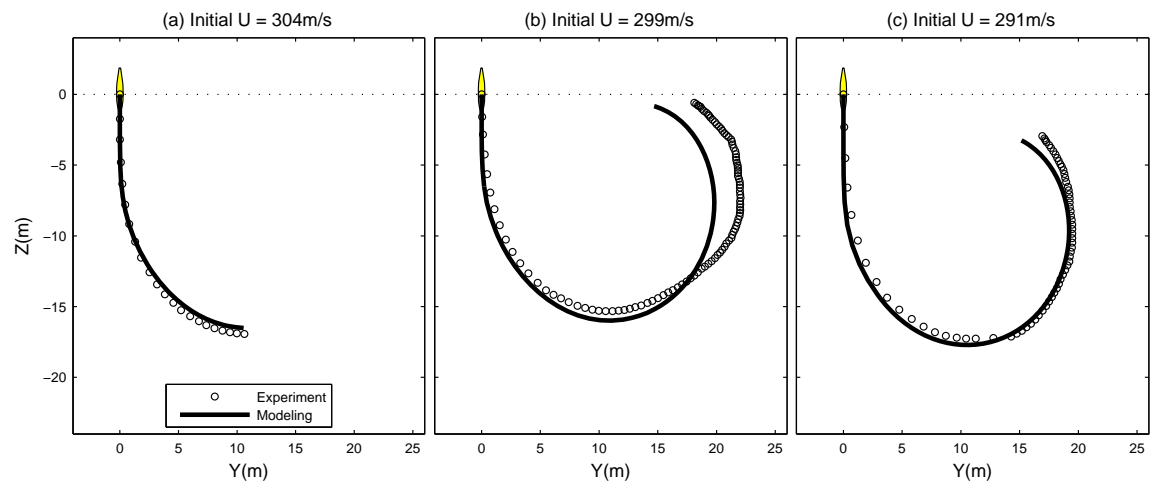


Fig. 16. Comparison between predicted and observed trajectories for Mk84 warhead with tail section and no fin (Type-1II) with initial water entry speed: (a) 304 ms^{-1} , (b) 298 ms^{-1} , and (c) 291 ms^{-1} .

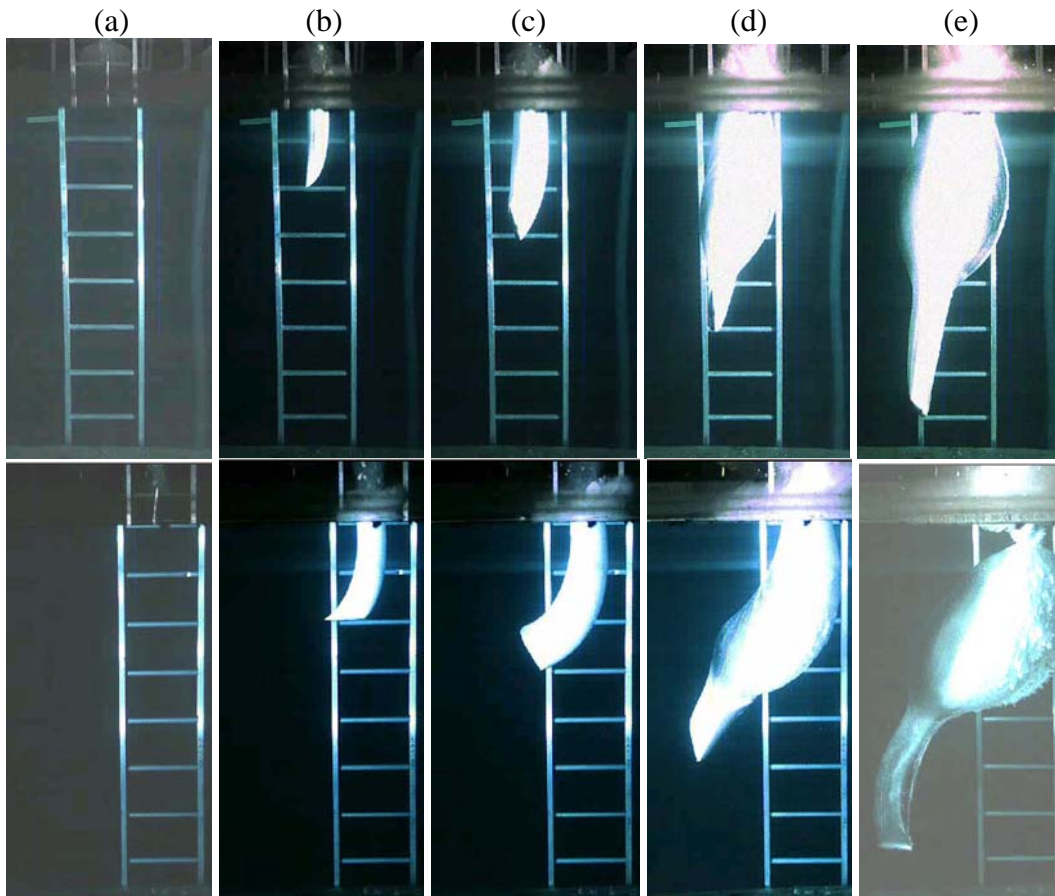


Fig. 17. Two HSV images for Launch-13 (Type-IV) at water entry velocity of 296 ms^{-1} : (a) initial water entry, (b) $t = 30.0 \text{ ms}$, (c) $t = 51.6 \text{ ms}$, (d) $t = 155.4 \text{ ms}$, and (e) $t = 418.2 \text{ ms}$.

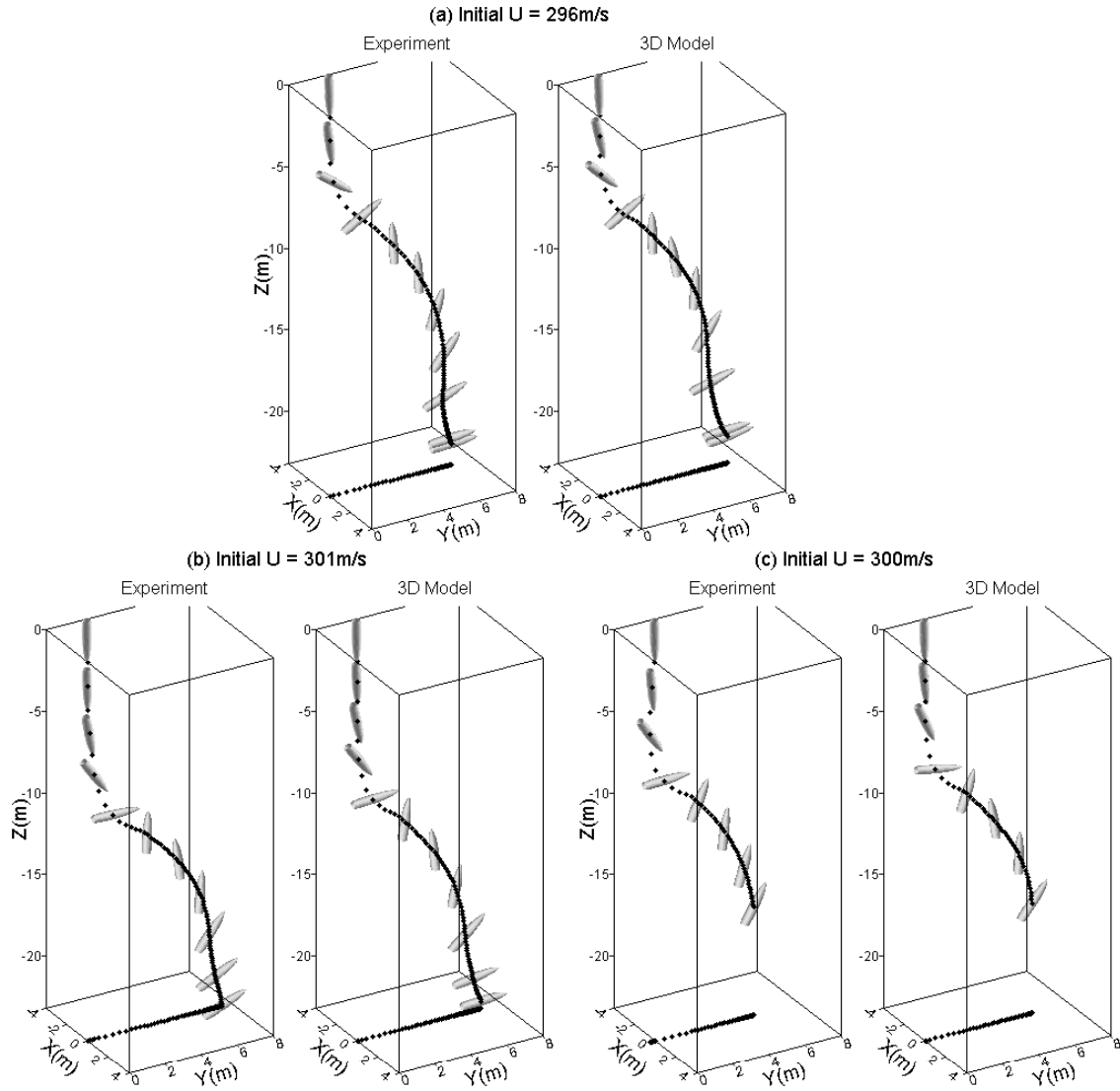


Fig. 18. Comparison between predicted and observed trajectories for Mk84 warhead with no tail section (Type-1V) with initial water entry speed: (a) 296 ms^{-1} , (b) 301 ms^{-1} , and (c) 301 ms^{-1} .

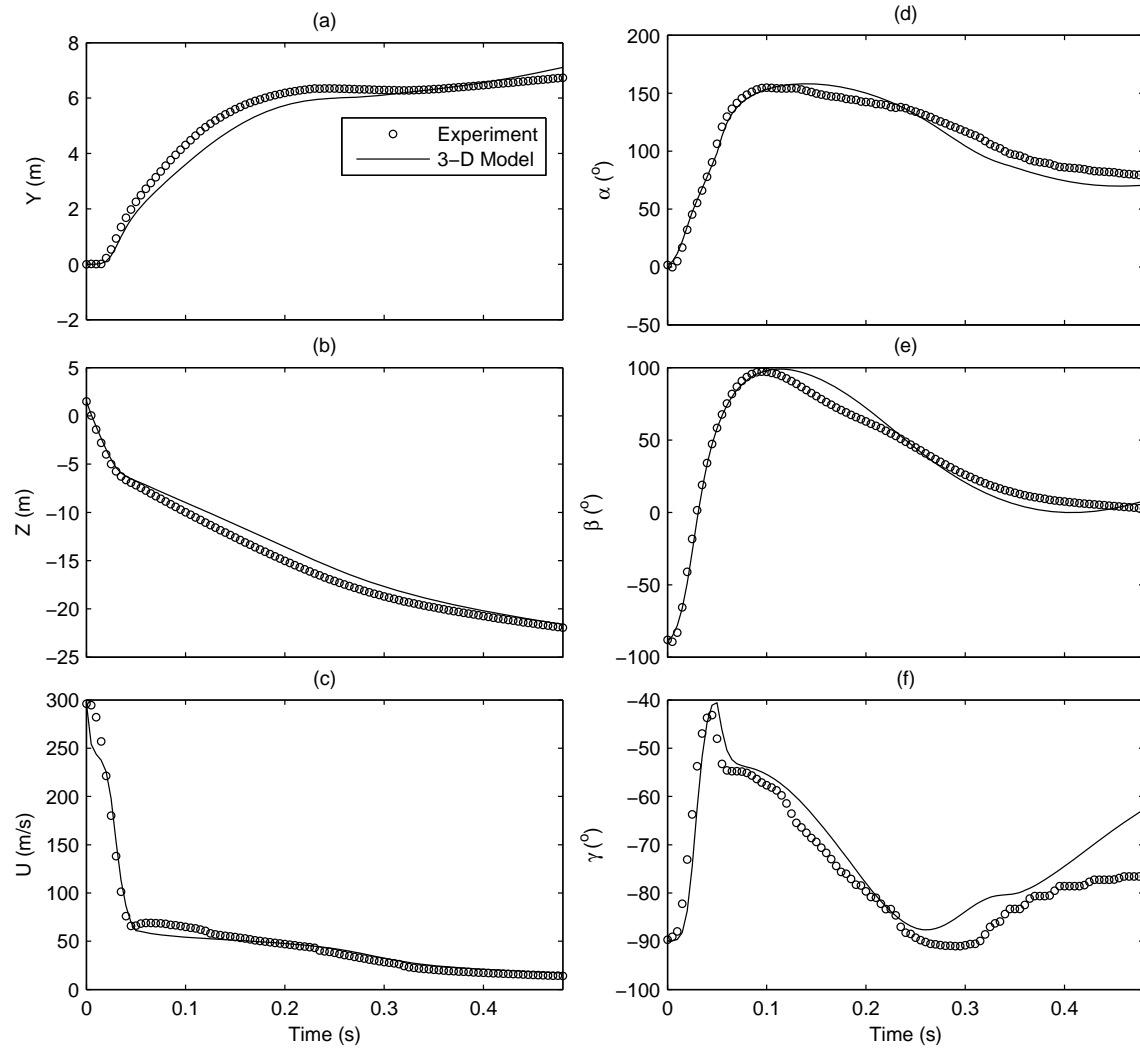


Fig. 19. Time-evolutions between predicted (solid) and observed (dotted) for Launch-13: (a) horizontal position (x) of o_m , (b) depth position (z) of o_m , (c) bomb speed (U), (d) angle γ , (e) angle β , and (f) attack angle α .

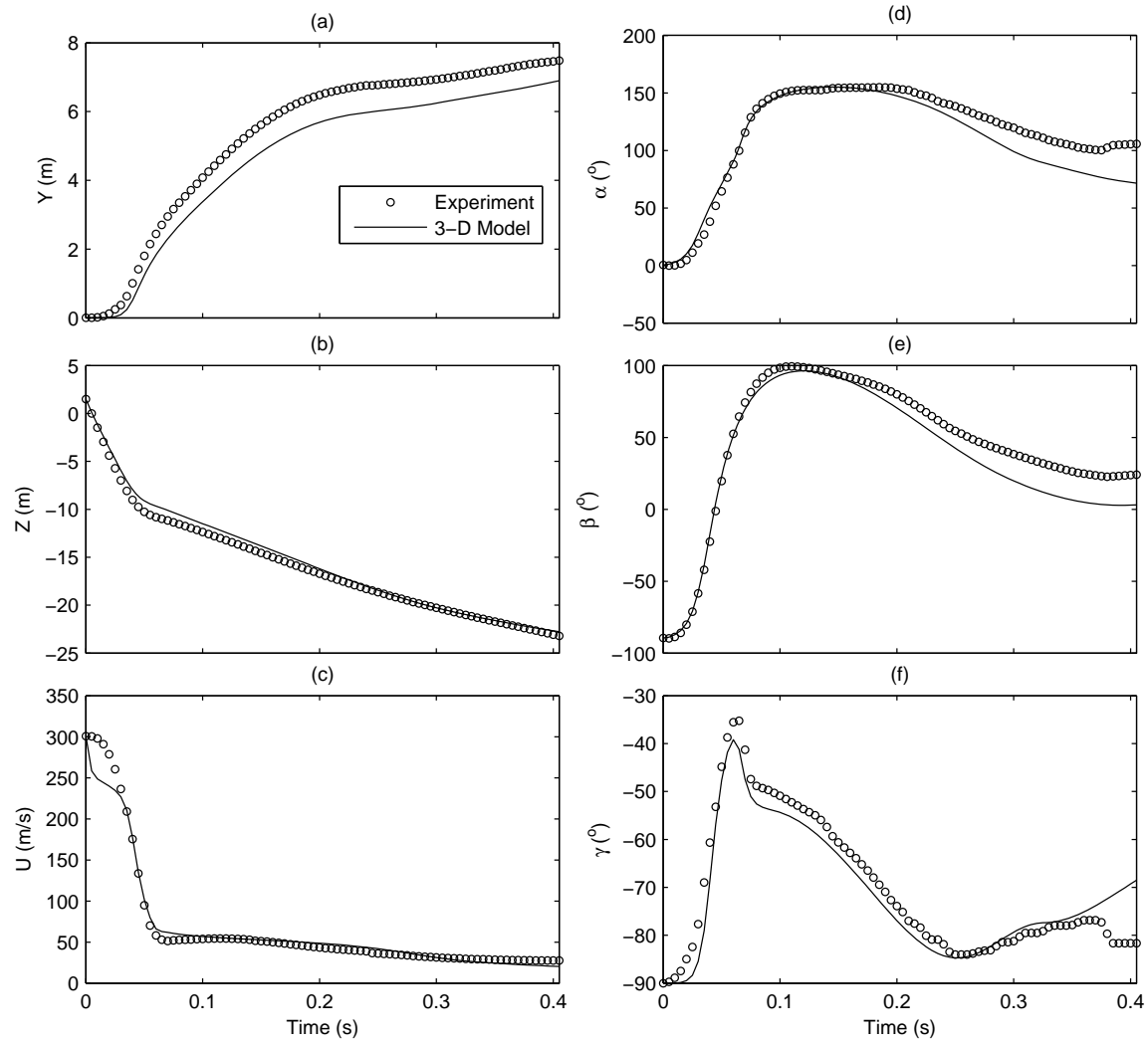


Fig. 20. Time-evolutions between predicted (solid) and observed (dotted) for Launch-14: (a) horizontal position (x) of o_m , (b) depth position (z) of o_m , (c) bomb speed (U), (d) angle γ , (e) angle β , and (f) attack angle α .

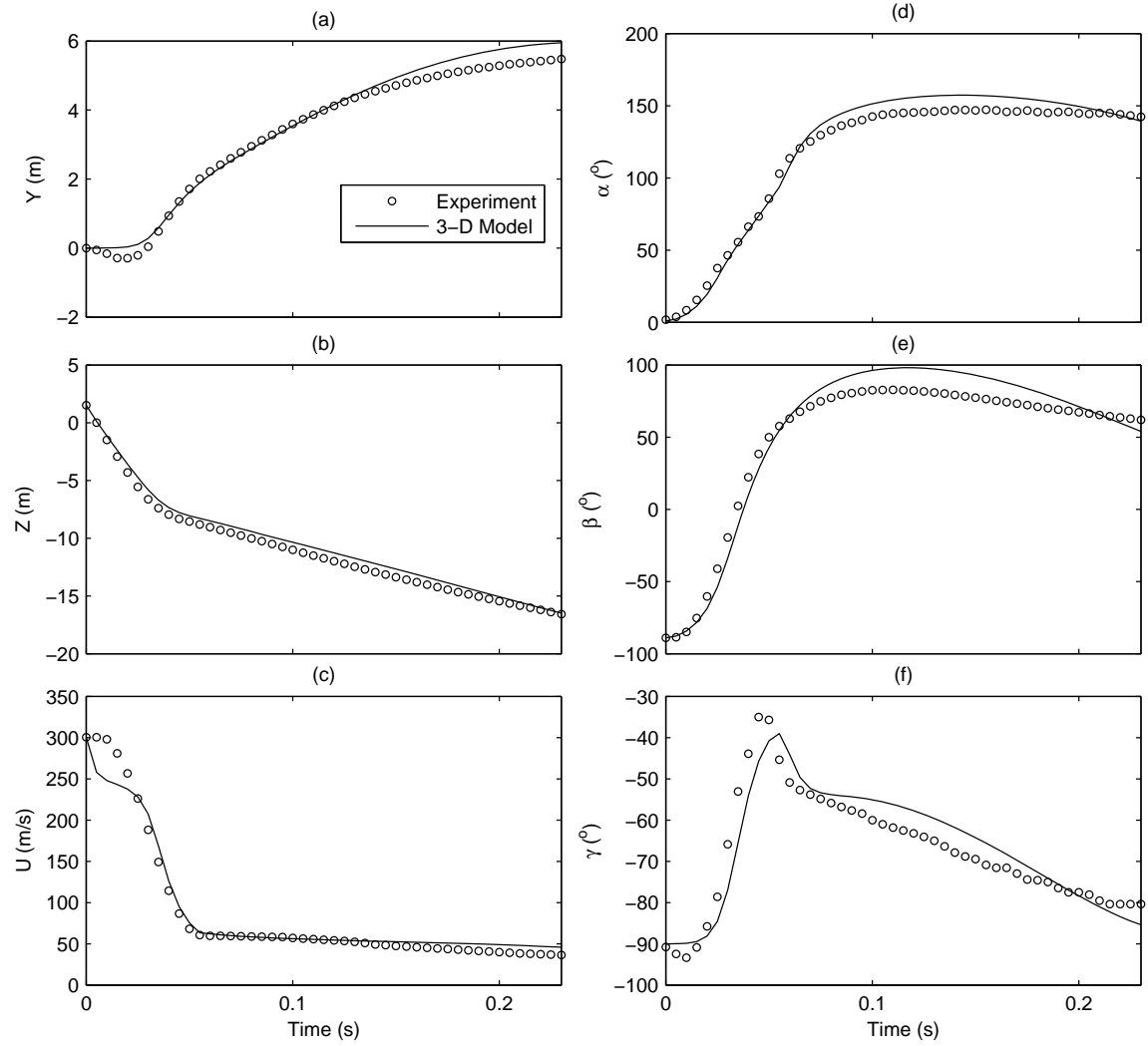


Fig. 21. Time-evolutions between predicted (solid) and observed (dotted) for Launch-15: (a) horizontal position (x) of o_m , (b) depth position (z) of o_m , (c) bomb speed (U), (d) angle γ , (e) angle β , and (f) attack angle α .

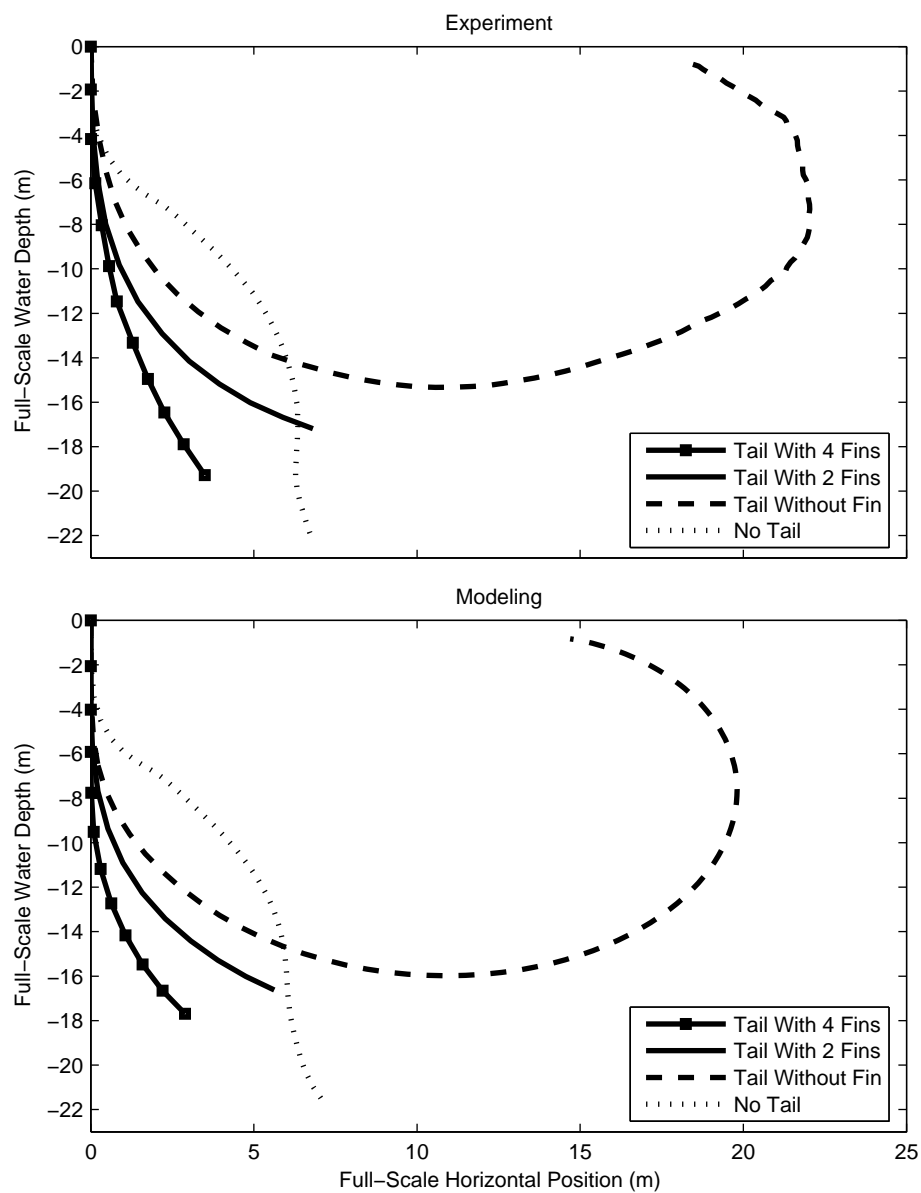


Fig. 22. Trajectories for Mk-84 warhead with different tail configurations.